Performance comparison between multi-frequency deterministic and probabilistic approaches

L. Poli, G. Oliveri, A. Massa

Abstract

This report is aimed to show a comparison between the probabilistic inversion methods based on single-task and multi-task Compressive Sensing (CS) strategies recast in a Bayesian framework and a deterministic technique of the state-of-the-art (a conjugate gradient-based method). The results show in particular the better capabilities of the multi-task CS method to take advantage of multi-frequency data when dealing with small-size scatterer in inverse scattering problems. The efficiency and robustness of such a method is validated considering different sparse-scatterer scenarios and different value of signal-to-noise ratio on the data.

Contents

Legenda

- SF-ST-BCS is the single-task Bayesian Compressive Sampling-based technique developed in [1] and working at a single frequency.
- MF-ST-BCS is the single-task Bayesian Compressive Sampling-based technique working at multiple frequencies.
- MF-MT-BCS is the multi-task Bayesian Compressive Sampling-based technique that exploits the correlation between multiple illumination frequencies.
- MF-CG is the Conjugate Gradient method working at multiple frequencies.

Comparison with MF-CG

0.1 Homogeneous Objects

0.1.1 Two Strips of Sides $l_1 = 0.16\lambda$, $l_2 = 0.50\lambda$

Goal: show the performances of the multi-frequency $MT - BCS$ when dealing with a sparse scatterer

- Number of frequencies F
- Number of Views: V
- Number of Measurements: M
- Number of Cells for the Inversion: N
- Number of Cells for the Direct solver: D
- Side of the investigation domain: L

Test Case Description

Direct solver:

- Square domain divided in $\sqrt{D} \times \sqrt{D}$ cells
- Domain side: $L = 3\lambda$ (at the central frequency)
- $D = 1296$ (discretization for the direct solver: $< \lambda/10$)

Investigation domain:

- Square domain divided in $\sqrt{N} \times \sqrt{N}$ cells
- $L = 3\lambda$
- $2ka = 2 \times \frac{2\pi}{\lambda} \times \frac{L\sqrt{2}}{2} = 6\pi\sqrt{2} = 26.65$
- $\#DOF = \frac{(2ka)^2}{2} = \frac{(2\times\frac{2\pi}{\lambda}\times\frac{L\sqrt{2}}{2})^2}{2} = 4\pi^2\left(\frac{L}{\lambda}\right)^2 = 4\pi^2 \times 9 \approx 355.3$
- N scelto in modo da essere vicino a $\#DOF$: $N = 324$ (18×18)

Measurement domain:

- Measurement points taken on a circle of radius $\rho = 3\lambda$ (at the central frequency)
- $M \approx 2ka \rightarrow M = 27$

Sources:

- $V = 1$ $(\theta = 0°)$
- Amplitude: $A = 1$ (plane waves)
- Number of Frequencies: $F = 11$
- Frequency Range: $I_F = [150\,Mhz : 450MHz]$ - Frequency Step: $S_F = [30\,Mhz]$

Object:

- Two strips of sides $l_1 = 0.16\lambda$, $l_2 = 0.50\lambda$
- $\varepsilon_r = 2.0$
- $\sigma = 0$ [S/m]

MT-BCS parameters:

- Gamma prior on noise variance parameters: $\beta_1 = 6.5 \times 10^{-1}$, $\beta_2 = 5.8 \times 10^{-2}$
- Convergenze parameter: $\tau = 1.0 \times 10^{-8}$

Two Homogeneous Strips of Sides $l_1 = 0.16\lambda$, $l_2 = 0.50\lambda$ - $\varepsilon_r = 1.5$ - BCS/CG Reconstructions Comparison

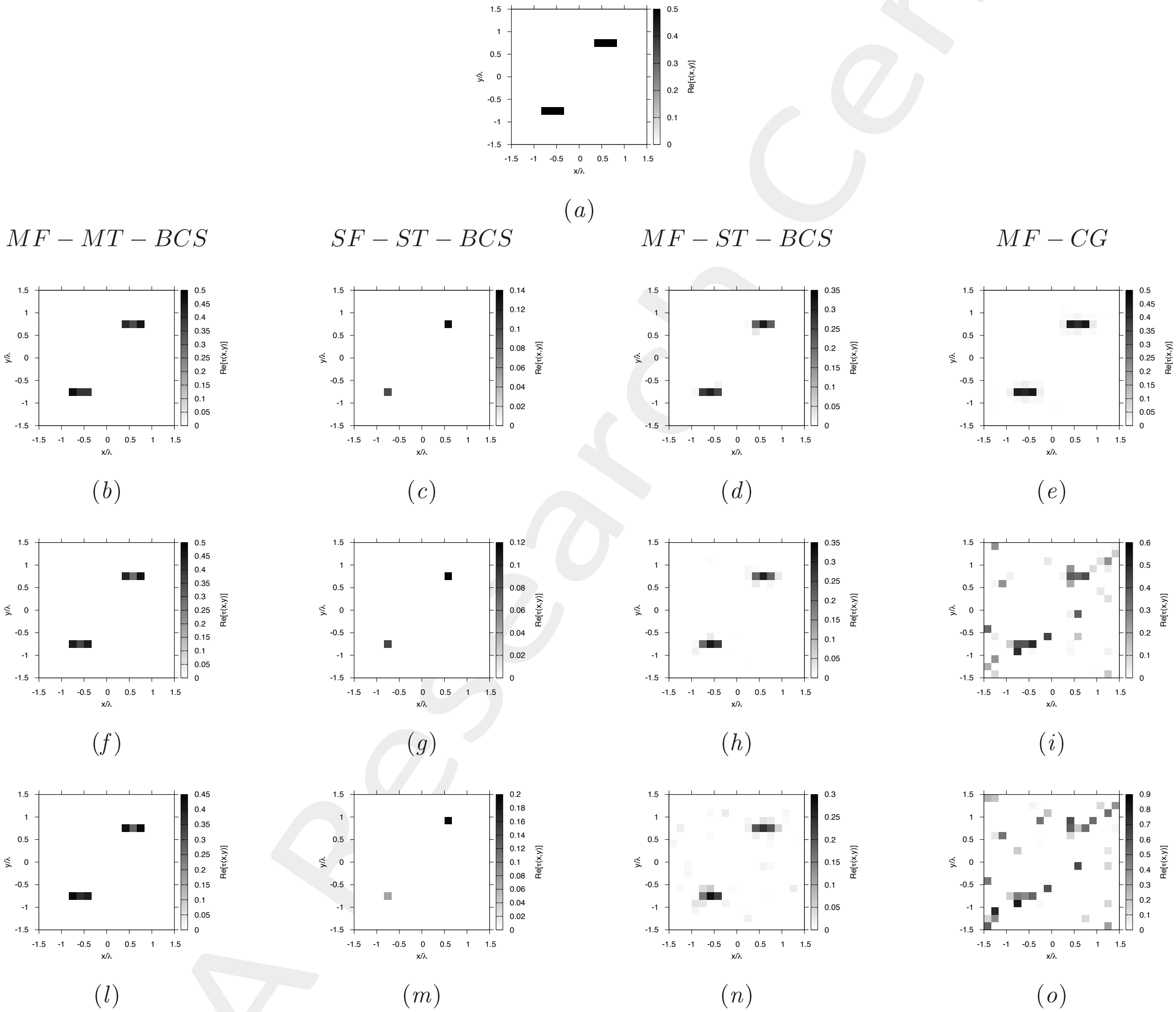

Figure 91. Actual object (a), $MF-MT-BCS$ $(b)(f)(l)$, $SF-ST-BCS$ $(c)(g)(m)$,$MF-ST-BCS$ $(d)(h)(n)$ and $MF-CG$ $(e)(i)(o)$ reconstructed object for $SNR = 50$ [dB] $(b)(c)(d)(e)$, $SNR = 10$ [dB] $(f)(g)(h)(i)$ and $SNR = 5$ [dB] $(l)(m)(n)(o)$.

Two Homogeneous Strips of Sides $l_1 = 0.16\lambda$, $l_2 = 0.50\lambda$ - $\varepsilon_r = 2.0$ - BCS/CG Reconstructions Comparison

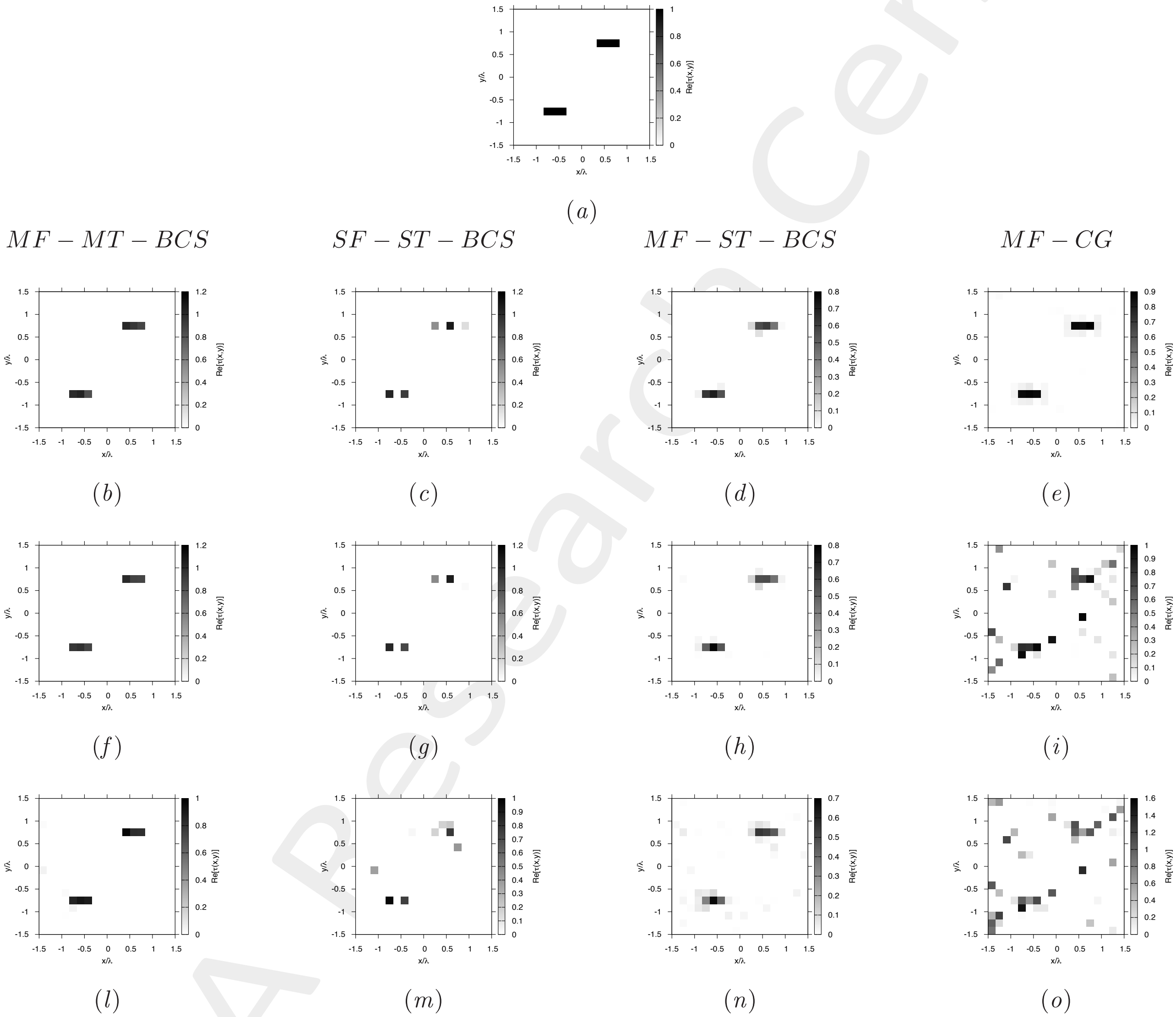

Figure 92. Actual object (a), $MF-MT-BCS$ $(b)(f)(l)$, $SF-ST-BCS$ $(c)(g)(m)$,$MF-ST-BCS$ $(d)(h)(n)$ and $MF-CG$ $(e)(i)(o)$ reconstructed object for $SNR = 50$ [dB] $(b)(c)(d)(e)$, $SNR = 10$ [dB] $(f)(g)(h)(i)$ and $SNR = 5$ [dB] $(l)(m)(n)(o)$.

Two Homogeneous Strips of Sides $l_1 = 0.16\lambda$, $l_2 = 0.50\lambda$ - $\varepsilon_r = 3.0$ - BCS/CG Reconstructions Comparison

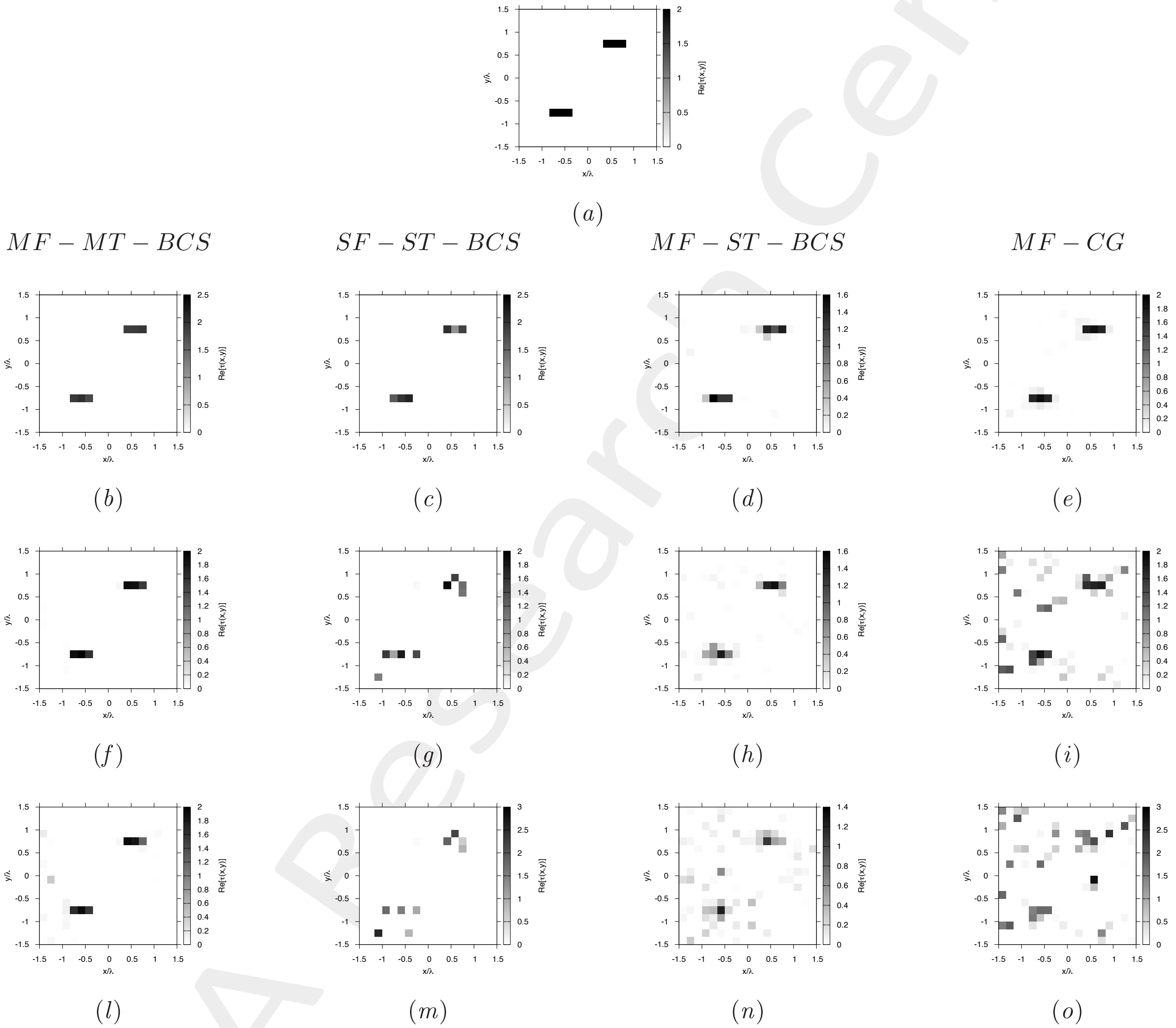

Figure 93. Actual object (a), $MF-MT-BCS$ $(b)(f)(l)$, $SF-ST-BCS$ $(c)(g)(m)$,$MF-ST-BCS$ $(d)(h)(n)$ and $MF-CG$ $(e)(i)(o)$ reconstructed object for $SNR = 50$ [dB] $(b)(c)(d)(e)$, $SNR = 10$ [dB] $(f)(g)(h)(i)$ and $SNR = 5$ [dB] $(l)(m)(n)(o)$.

Two Homogeneous Strips of Sides $l_1 = 0.16\lambda$, $l_2 = 0.50\lambda$ - $\varepsilon_r = 5.0$ - BCS/CG Reconstructions Comparison

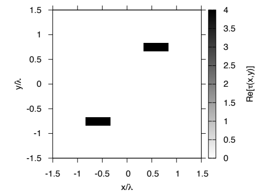

(a)

$MF-MT-BCS$ | $SF-ST-BCS$ | $MF-ST-BCS$ | $MF-CG$

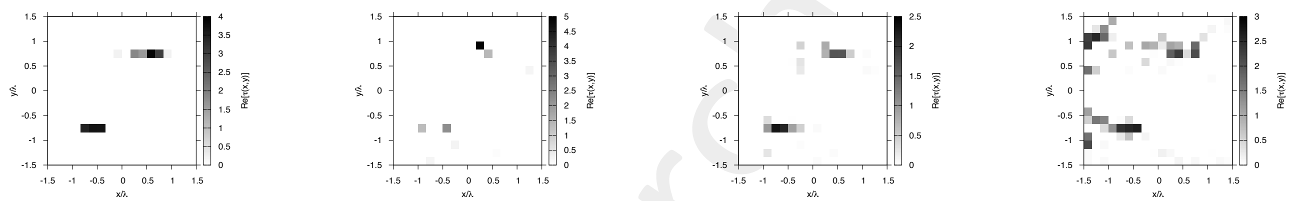

(b) (c) (d) (e)

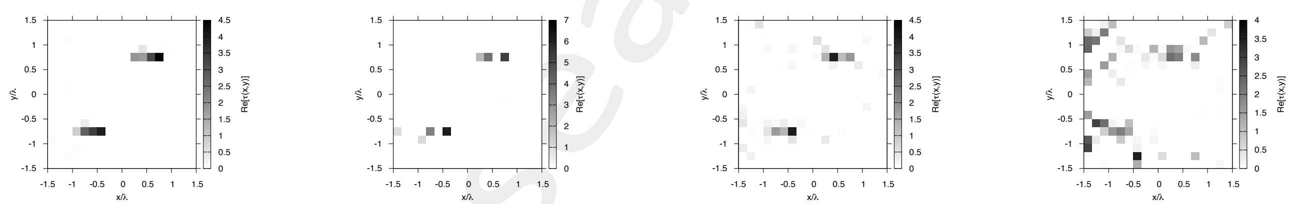

(f) (g) (h) (i)

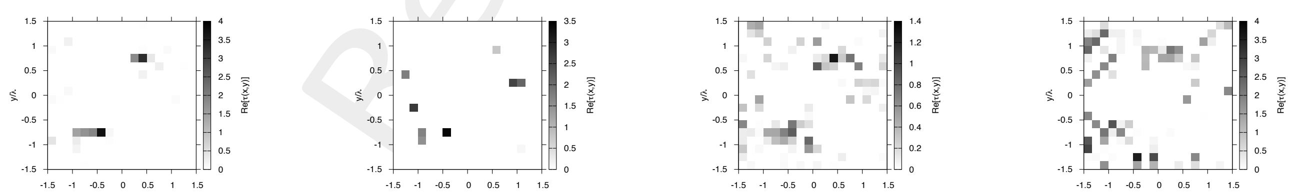

(l) (m) (n) (o)

Figure 94. Actual object (a), $MF-MT-BCS$ $(b)(f)(l)$, $SF-ST-BCS$ $(c)(g)(m)$,$MF-ST-BCS$ $(d)(h)(n)$ and $MF-CG$ $(e)(i)(o)$ reconstructed object for $SNR = 50$ [dB] $(b)(c)(d)(e)$, $SNR = 10$ [dB] $(f)(g)(h)(i)$ and $SNR = 5$ [dB] $(l)(m)(n)(o)$.

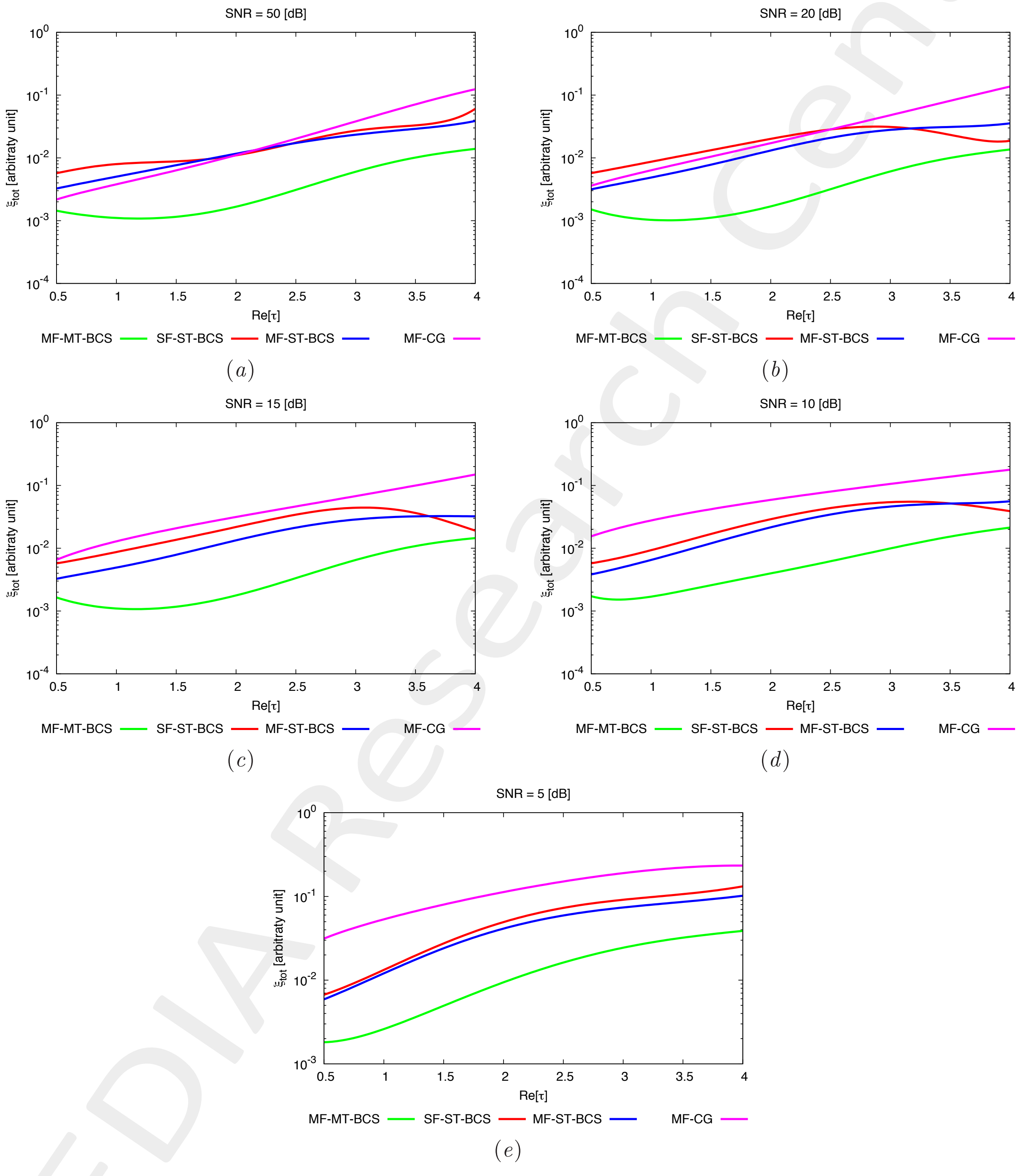

Figure 95. Behaviour of total error ξ_{tot} as a function of ε_r, for $SNR = 50$ [dB] (a), $SNR = 20$ [dB] (b), $SNR = 15$ [dB] (c), $SNR = 10$ [dB] (d) and $SNR = 5$ [dB] (e).

Two Homogeneous Strips of Sides $l_1 = 0.16\lambda$, $l_2 = 0.50\lambda$ - BCS/CG Errors vs. SNR Comparison

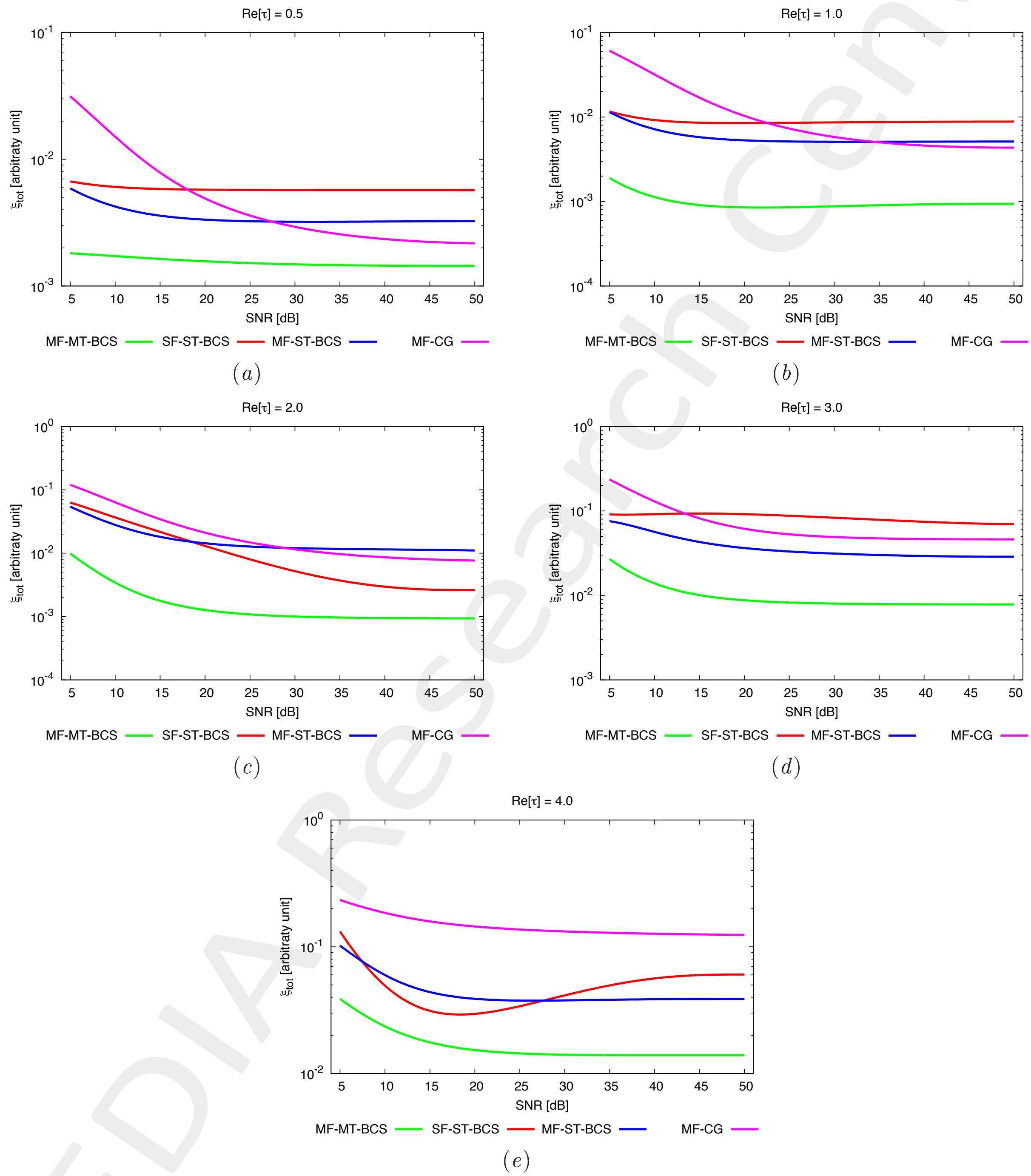

Figure 96. Behaviour of total error ξ_{tot} as a function of SNR, for $\varepsilon_r = 1.5$ [dB] (a), $\varepsilon_r = 2.0$ [dB] (b), $\varepsilon_r = 3.0$ [dB] (c), $\varepsilon_r = 4.0$ [dB] (d) and $\varepsilon_r = 5.0$ [dB] (e).

0.1.2 Eight Pixels of Side $l = 0.16\lambda$

Goal: show the performances of the multi-frequency $MT - BCS$ when dealing with a sparse scatterer

- Number of frequencies F
- Number of Views: V
- Number of Measurements: M
- Number of Cells for the Inversion: N
- Number of Cells for the Direct solver: D
- Side of the investigation domain: L

Test Case Description

Direct solver:

- Square domain divided in $\sqrt{D} \times \sqrt{D}$ cells
- Domain side: $L = 3\lambda$ (at the central frequency)
- $D = 1296$ (discretization for the direct solver: $< \lambda/10$)

Investigation domain:

- Square domain divided in $\sqrt{N} \times \sqrt{N}$ cells
- $L = 3\lambda$
- $2ka = 2 \times \frac{2\pi}{\lambda} \times \frac{L\sqrt{2}}{2} = 6\pi\sqrt{2} = 26.65$
- $\#DOF = \frac{(2ka)^2}{2} = \frac{(2 \times \frac{2\pi}{\lambda} \times \frac{L\sqrt{2}}{2})^2}{2} = 4\pi^2 \left(\frac{L}{\lambda}\right)^2 = 4\pi^2 \times 9 \approx 355.3$
- N scelto in modo da essere vicino a $\#DOF$: $N = 324$ (18×18)

Measurement domain:

- Measurement points taken on a circle of radius $\rho = 3\lambda$ (at the central frequency)
- $M \approx 2ka \rightarrow M = 27$

Sources:

- $V = 1$ $(\theta = 0°)$
- Amplitude: $A = 1$ (plane waves)
- Number of Frequencies: $F = 11$
- Frequency Range: $I_F = [150\,Mhz : 450MHz]$ - Frequency Step: $S_F = [30\,Mhz]$

Object:

- Eight square cylinders of side $l = 0.16\lambda$
- $\varepsilon_r = 2.0$
- $\sigma = 0$ [S/m]

MT-BCS parameters:

- Gamma prior on noise variance parameters: $\beta_1 = 6.5 \times 10^{-1}$, $\beta_2 = 5.8 \times 10^{-2}$
- Convergenze parameter: $\tau = 1.0 \times 10^{-8}$

Eight Homogeneous Pixels of Side $l = 0.16\lambda$ - $\varepsilon_r = 1.5$ - BCS/CG Reconstructions Comparison

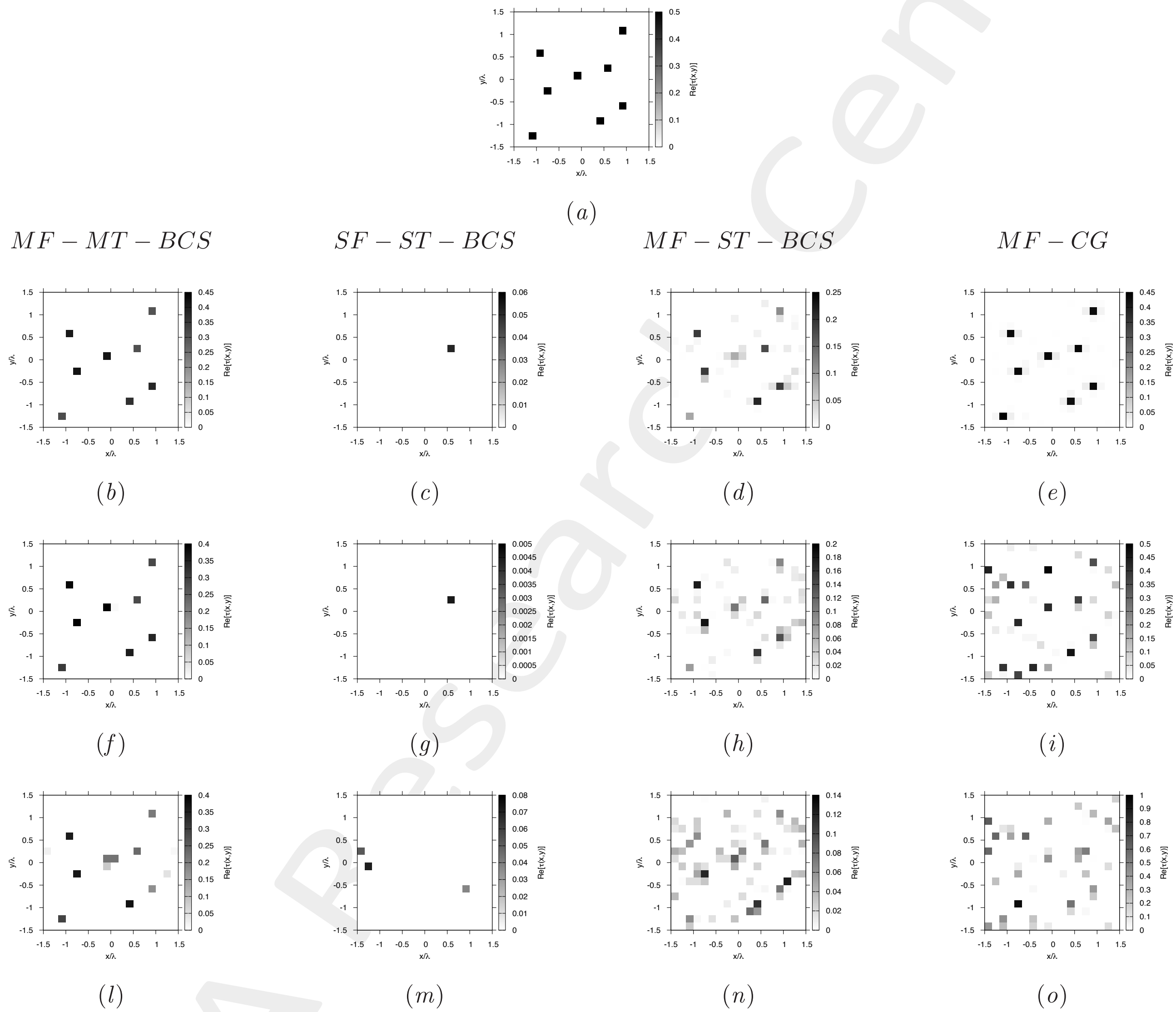

Figure 97. Actual object (a), $MF-MT-BCS$ $(b)(f)(l)$, $SF-ST-BCS$ $(c)(g)(m)$,$MF-ST-BCS$ $(d)(h)(n)$ and $MF-CG$ $(e)(i)(o)$ reconstructed object for $SNR = 50$ [dB] $(b)(c)(d)(e)$, $SNR = 10$ [dB] $(f)(g)(h)(i)$ and $SNR = 5$ [dB] $(l)(m)(n)(o)$.

Eight Homogeneous Pixels of Side $l = 0.16\lambda$ - $\varepsilon_r = 2.0$ - BCS/CG Reconstructions Comparison

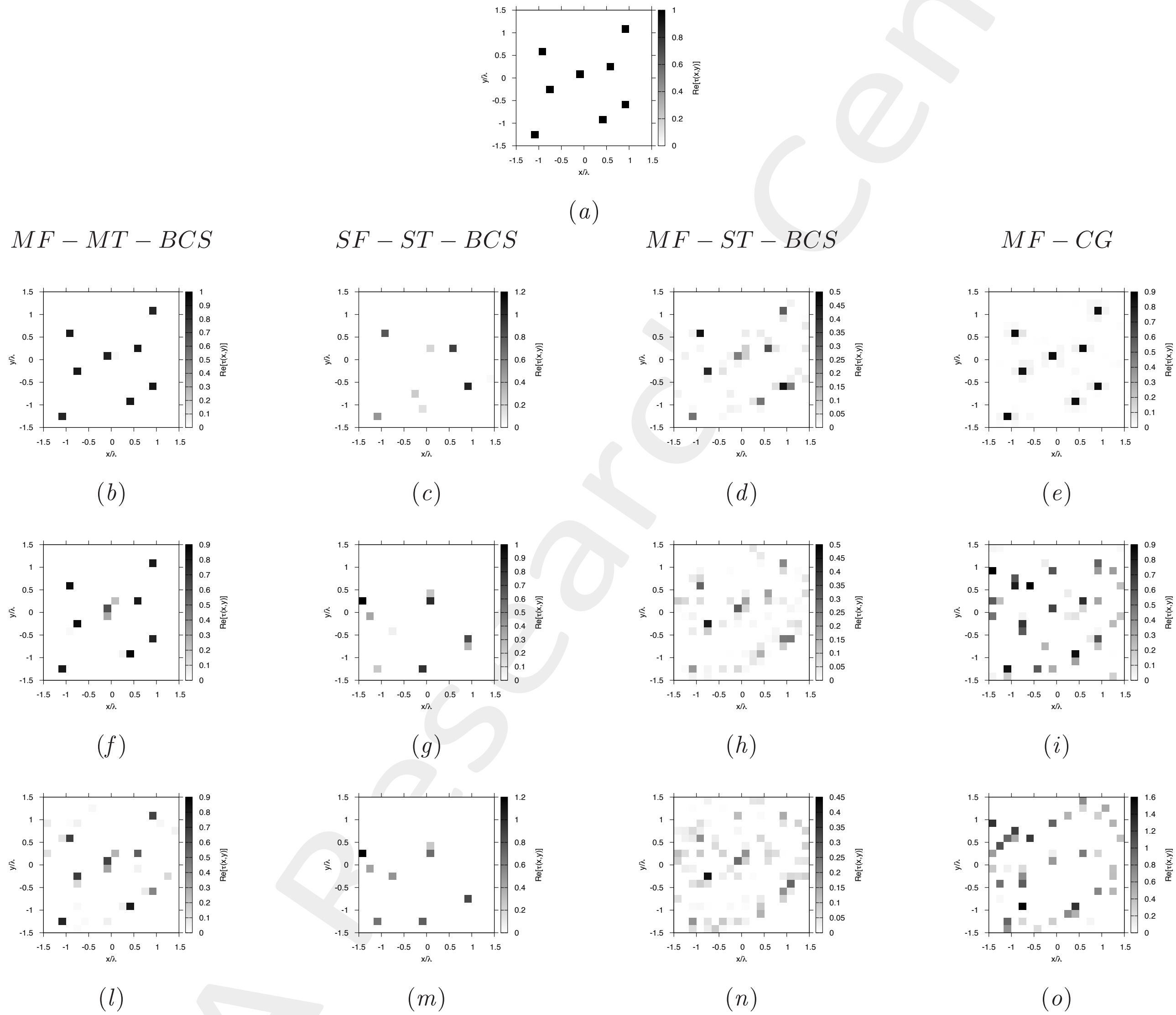

Figure 98. Actual object (a), $MF-MT-BCS$ $(b)(f)(l)$, $SF-ST-BCS$ $(c)(g)(m)$,$MF-ST-BCS$ $(d)(h)(n)$ and $MF-CG$ $(e)(i)(o)$ reconstructed object for $SNR = 50$ [dB] $(b)(c)(d)(e)$, $SNR = 10$ [dB] $(f)(g)(h)(i)$ and $SNR = 5$ [dB] $(l)(m)(n)(o)$.

Eight Homogeneous Pixels of Side $l = 0.16\lambda$ - $\varepsilon_r = 3.0$ - BCS/CG Reconstructions Comparison

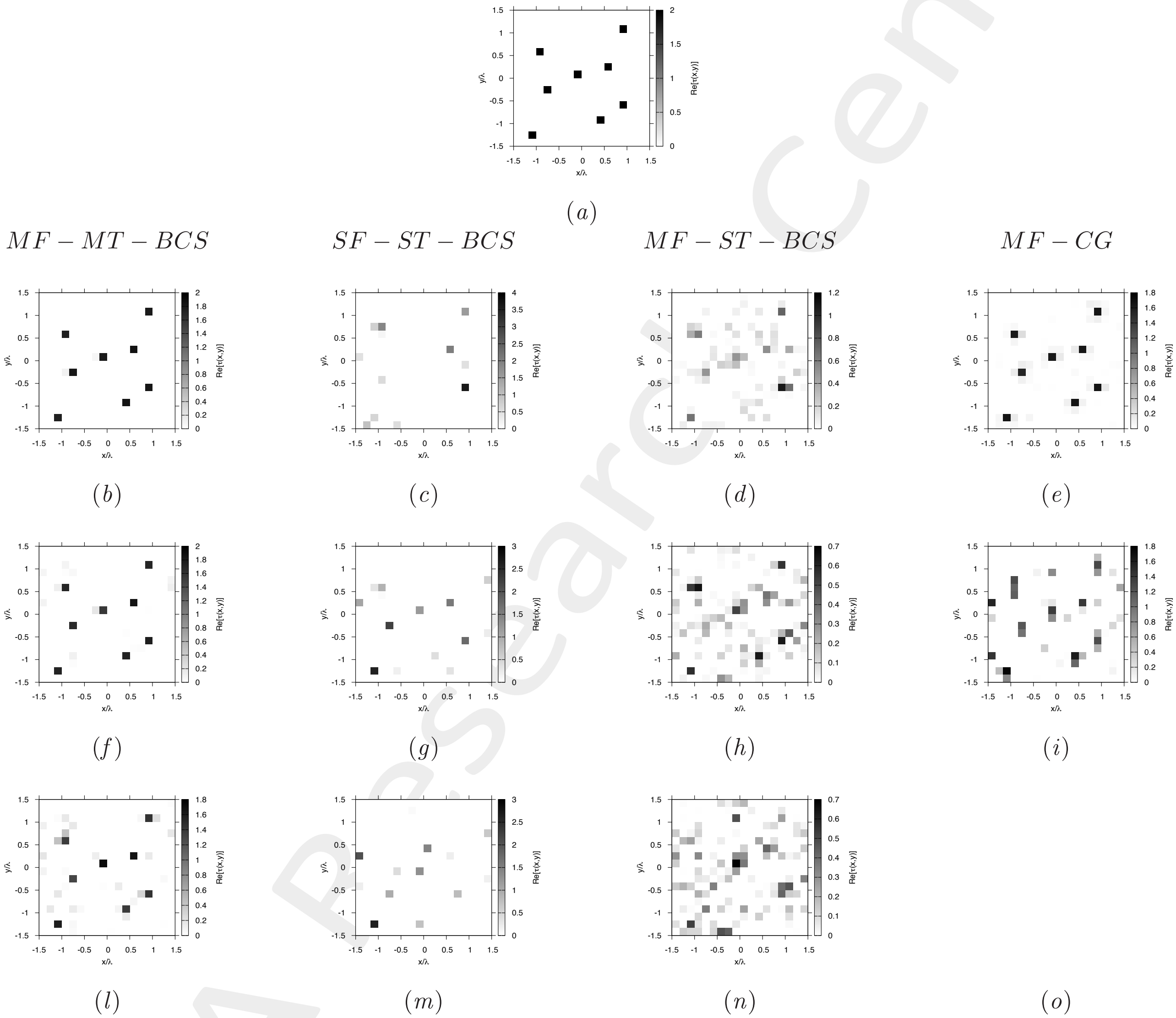

Figure 99. Actual object (a), $MF-MT-BCS$ $(b)(f)(l)$, $SF-ST-BCS$ $(c)(g)(m)$,$MF-ST-BCS$ $(d)(h)(n)$ and $MF-CG$ $(e)(i)(o)$ reconstructed object for $SNR = 50$ [dB] $(b)(c)(d)(e)$, $SNR = 10$ [dB] $(f)(g)(h)(i)$ and $SNR = 5$ [dB] $(l)(m)(n)(o)$.

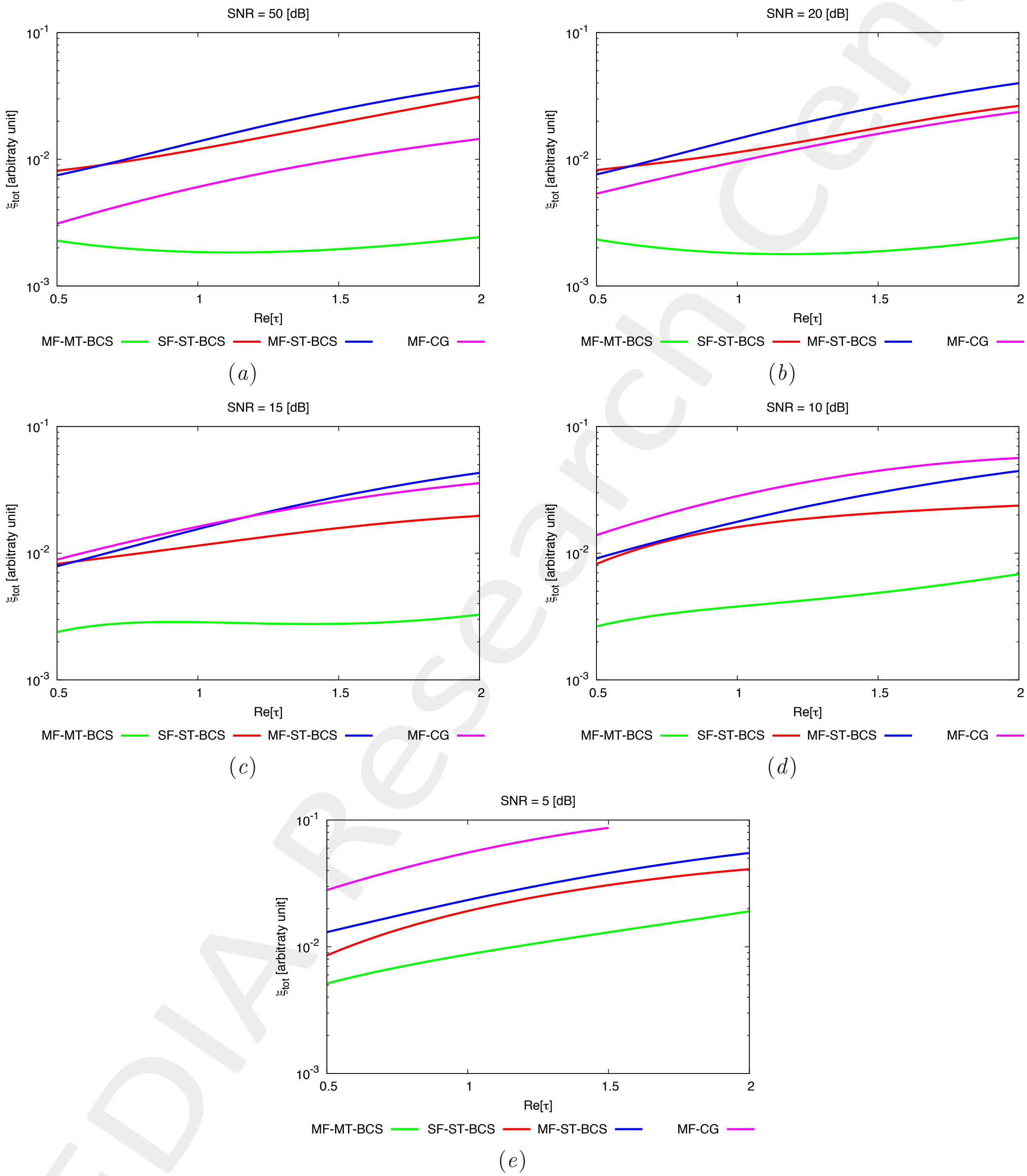

Figure 100. Behaviour of total error ξ_{tot} as a function of ε_r, for $SNR = 50$ [dB] (a), $SNR = 20$ [dB] (b), $SNR = 15$ [dB] (c), $SNR = 10$ [dB] (d) and $SNR = 5$ [dB] (e).

Eight Homogeneous Pixels of Side $l = 0.16\lambda$ - BCS/CG Errors vs. SNR Comparison

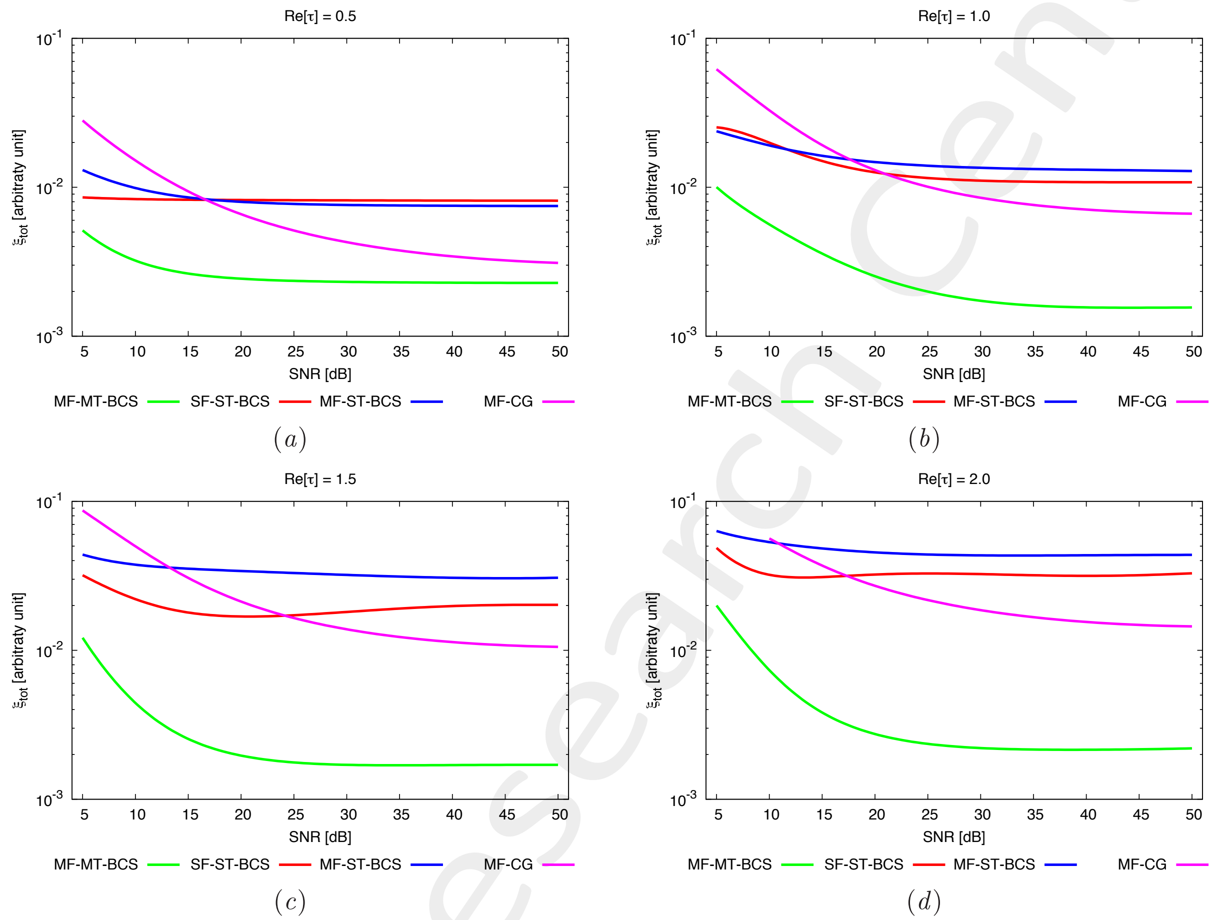

Figure 101. Behaviour of total error ξ_{tot} as a function of SNR, for $\varepsilon_r = 1.5$ [dB] (a), $\varepsilon_r = 2.0$ [dB] (b), $\varepsilon_r = 2.5$ [dB] (c) and $\varepsilon_r = 3.0$ [dB].

0.1.3 Rectangle of Sides $l_1 = 0.66\lambda$, $l_2 = 0.33\lambda$

Goal: show the performances of the multi-frequency $MT-BCS$ when dealing with a sparse scatterer

- Number of frequencies F
- Number of Views: V
- Number of Measurements: M
- Number of Cells for the Inversion: N
- Number of Cells for the Direct solver: D
- Side of the investigation domain: L

Test Case Description

Direct solver:

- Square domain divided in $\sqrt{D} \times \sqrt{D}$ cells
- Domain side: $L = 3\lambda$ (at the central frequency)
- $D = 1296$ (discretization for the direct solver: $< \lambda/10$)

Investigation domain:

- Square domain divided in $\sqrt{N} \times \sqrt{N}$ cells
- $L = 3\lambda$
- $2ka = 2 \times \frac{2\pi}{\lambda} \times \frac{L\sqrt{2}}{2} = 6\pi\sqrt{2} = 26.65$
- $\#DOF = \frac{(2ka)^2}{2} = \frac{(2\times\frac{2\pi}{\lambda}\times\frac{L\sqrt{2}}{2})^2}{2} = 4\pi^2\left(\frac{L}{\lambda}\right)^2 = 4\pi^2 \times 9 \approx 355.3$
- N scelto in modo da essere vicino a $\#DOF$: $N = 324$ (18×18)

Measurement domain:

- Measurement points taken on a circle of radius $\rho = 3\lambda$ (at the central frequency)
- $M \approx 2ka \rightarrow M = 27$

Sources:

- $V = 1$ $(\theta = 0°)$
- Amplitude: $A = 1$ (plane waves)
- Number of Frequencies: $F = 11$
- Frequency Range: $I_F = [150\,Mhz\,:\,450MHz]$ - Frequency Step: $S_F = [30\,Mhz]$

Object:

- Rectangle of sides $l_1 = 0.33\lambda$, $l_2 = 0.66\lambda$
- $\varepsilon_r = 2.0$
- $\sigma = 0$ [S/m]

BCS parameters:

- Gamma prior on noise variance parameters: $\beta_1 = 6.5 \times 10^{-1}$, $\beta_2 = 5.8 \times 10^{-2}$
- Convergenze parameter: $\tau = 1.0 \times 10^{-8}$

Homogeneous Rectangle of Sides $l_1 = 0.66\lambda$, $l_2 = 0.33\lambda$ - $\varepsilon_r = 1.5$ - BCS/CG Reconstructions Comparison

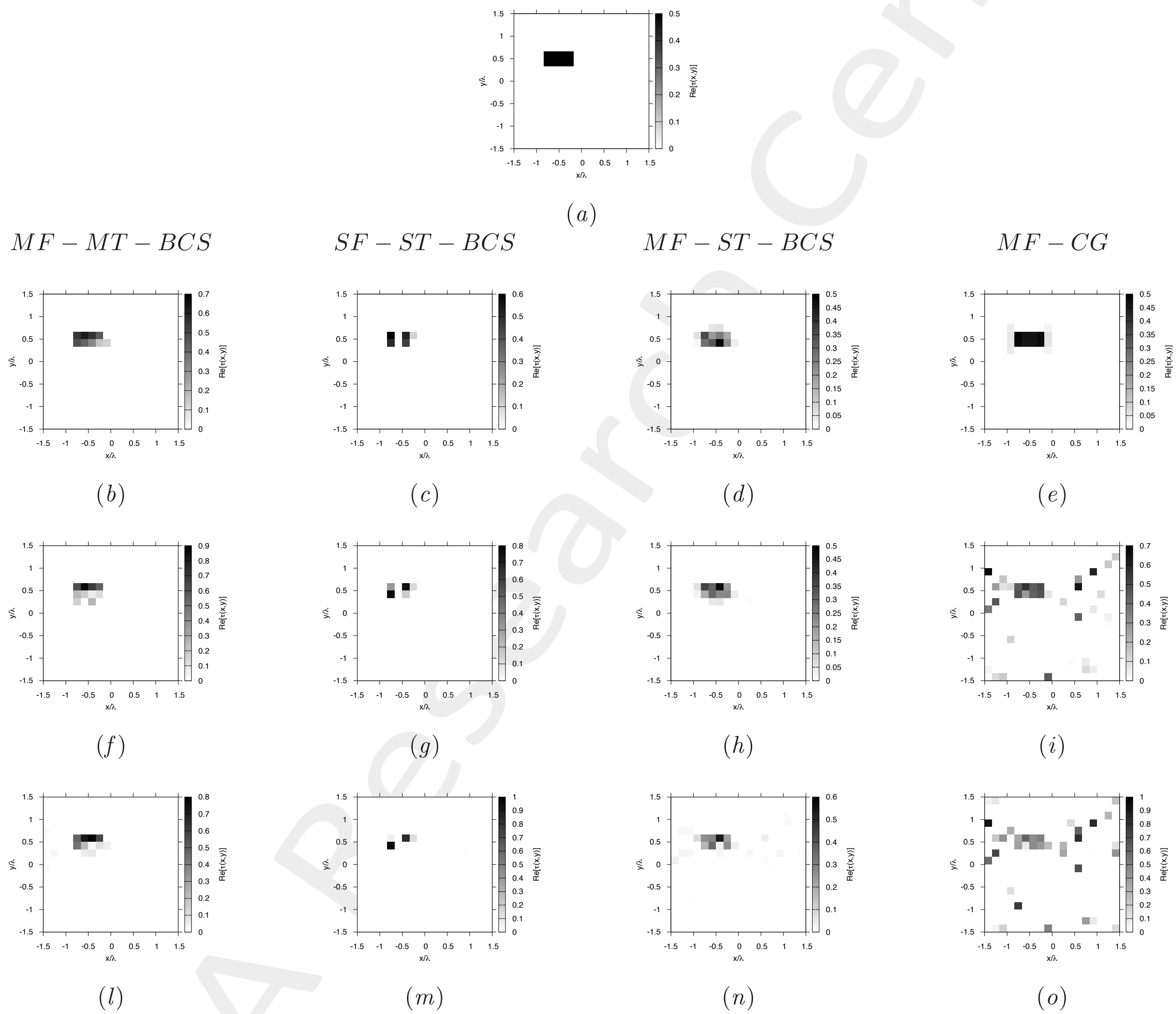

Figure 102. Actual object (a), $MF-MT-BCS$ $(b)(f)(l)$, $SF-ST-BCS$ $(c)(g)(m)$,$MF-ST-BCS$ $(d)(h)(n)$ and $MF-CG$ $(e)(i)(o)$ reconstructed object for $SNR=50$ [dB] $(b)(c)(d)(e)$, $SNR=10$ [dB] $(f)(g)(h)(i)$ and $SNR=5$ [dB] $(l)(m)(n)(o)$.

Homogeneous Rectangle of Sides $l_1 = 0.66\lambda$, $l_2 = 0.33\lambda$ - $\varepsilon_r = 2.0$ - BCS/CG Reconstructions Comparison

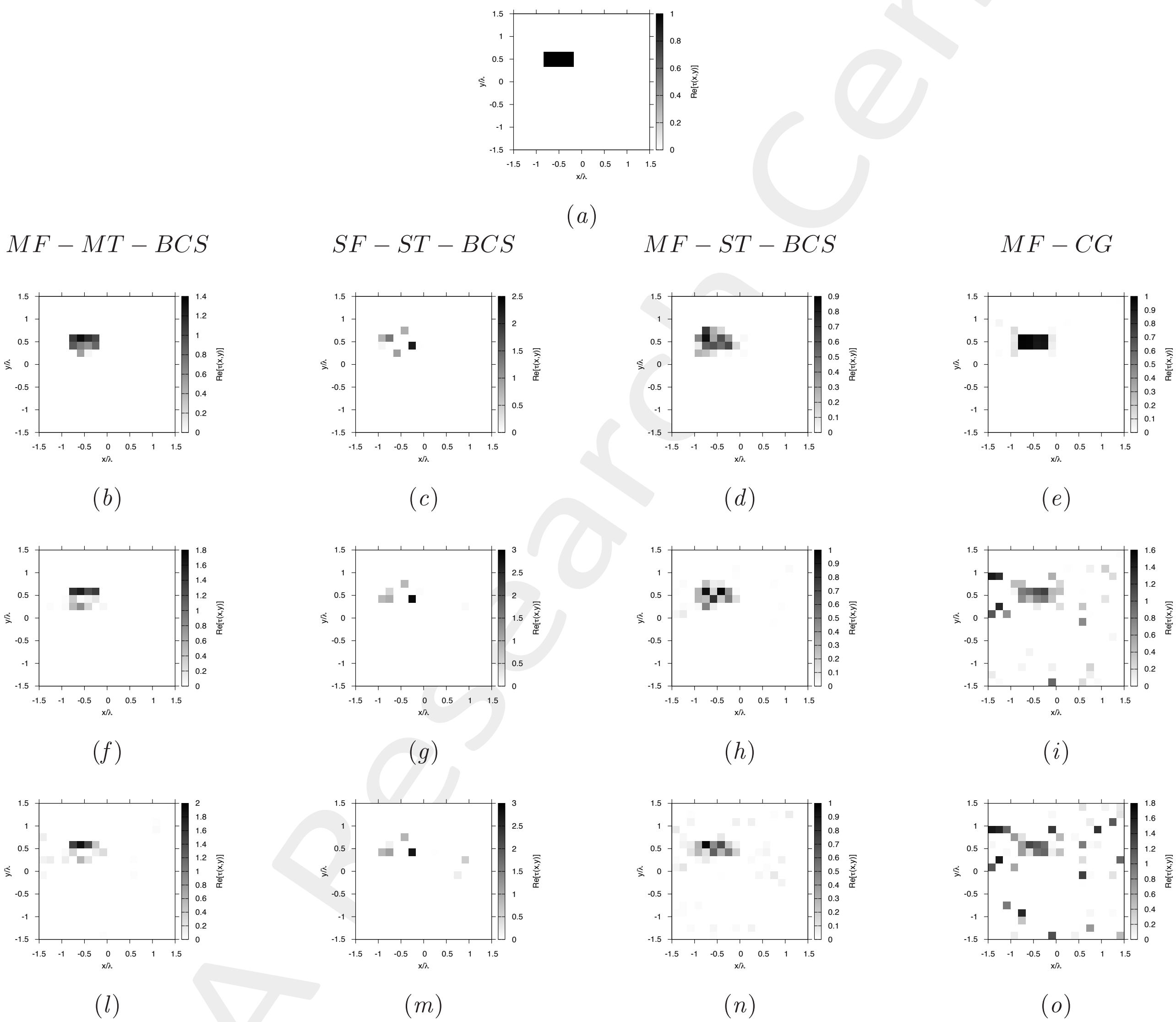

Figure 103. Actual object (a), $MF-MT-BCS$ $(b)(f)(l)$, $SF-ST-BCS$ $(c)(g)(m)$,$MF-ST-BCS$ $(d)(h)(n)$ and $MF-CG$ $(e)(i)(o)$ reconstructed object for $SNR = 50$ [dB] $(b)(c)(d)(e)$, $SNR = 10$ [dB] $(f)(g)(h)(i)$ and $SNR = 5$ [dB] $(l)(m)(n)(o)$.

Homogeneous Rectangle of Sides $l_1 = 0.66\lambda$, $l_2 = 0.33\lambda$ - $\varepsilon_r = 3.0$ - BCS/CG Reconstructions Comparison

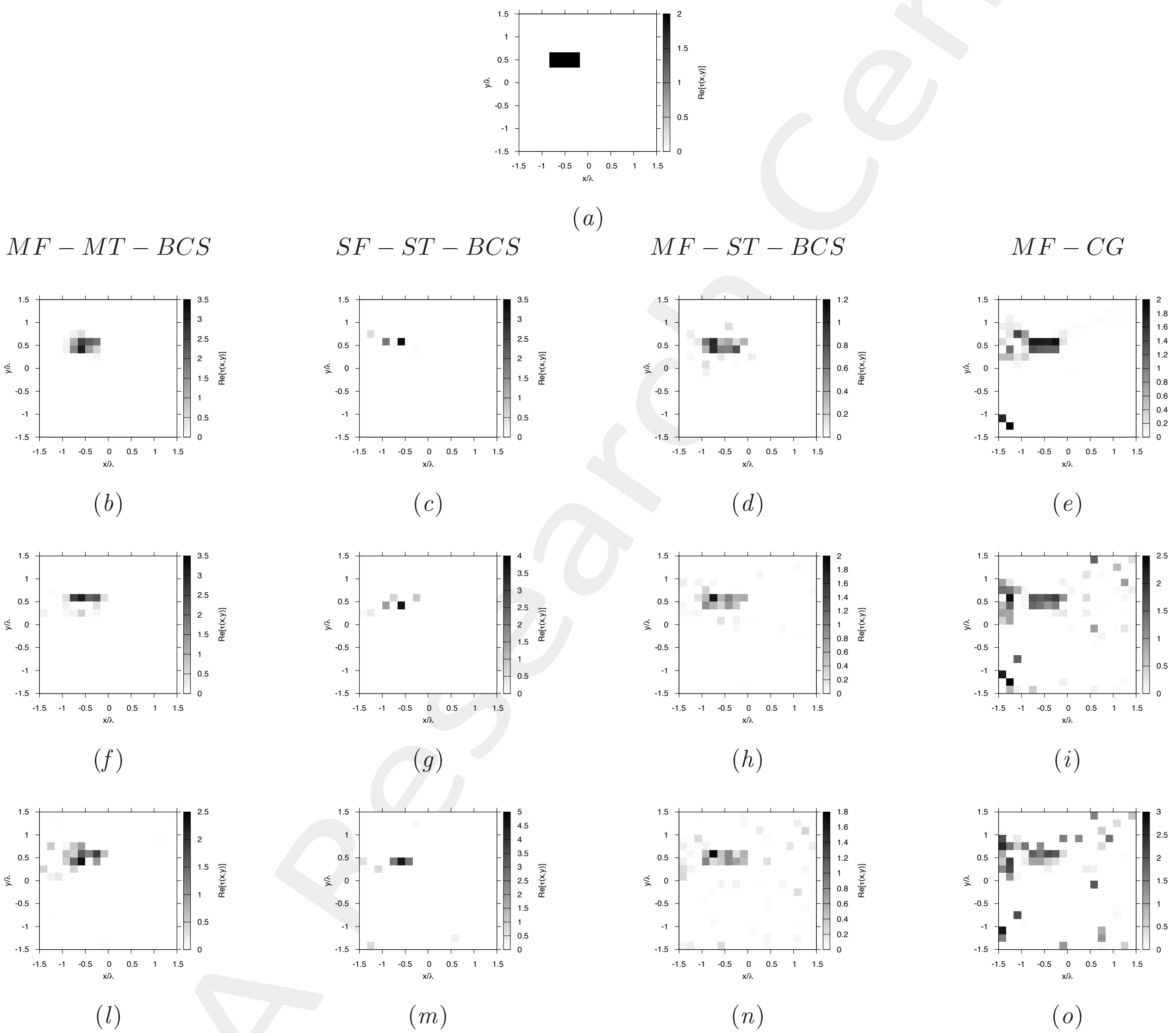

Figure 104. Actual object (a), $MF-MT-BCS$ $(b)(f)(l)$, $SF-ST-BCS$ $(c)(g)(m)$,$MF-ST-BCS$ $(d)(h)(n)$ and $MF-CG$ $(e)(i)(o)$ reconstructed object for $SNR = 50$ [dB] $(b)(c)(d)(e)$, $SNR = 10$ [dB] $(f)(g)(h)(i)$ and $SNR = 5$ [dB] $(l)(m)(n)(o)$.

Homogeneous Rectangle of Sides $l_1 = 0.66\lambda$, $l_2 = 0.33\lambda$ - BCS/CG Errors vs. ε_r Comparison

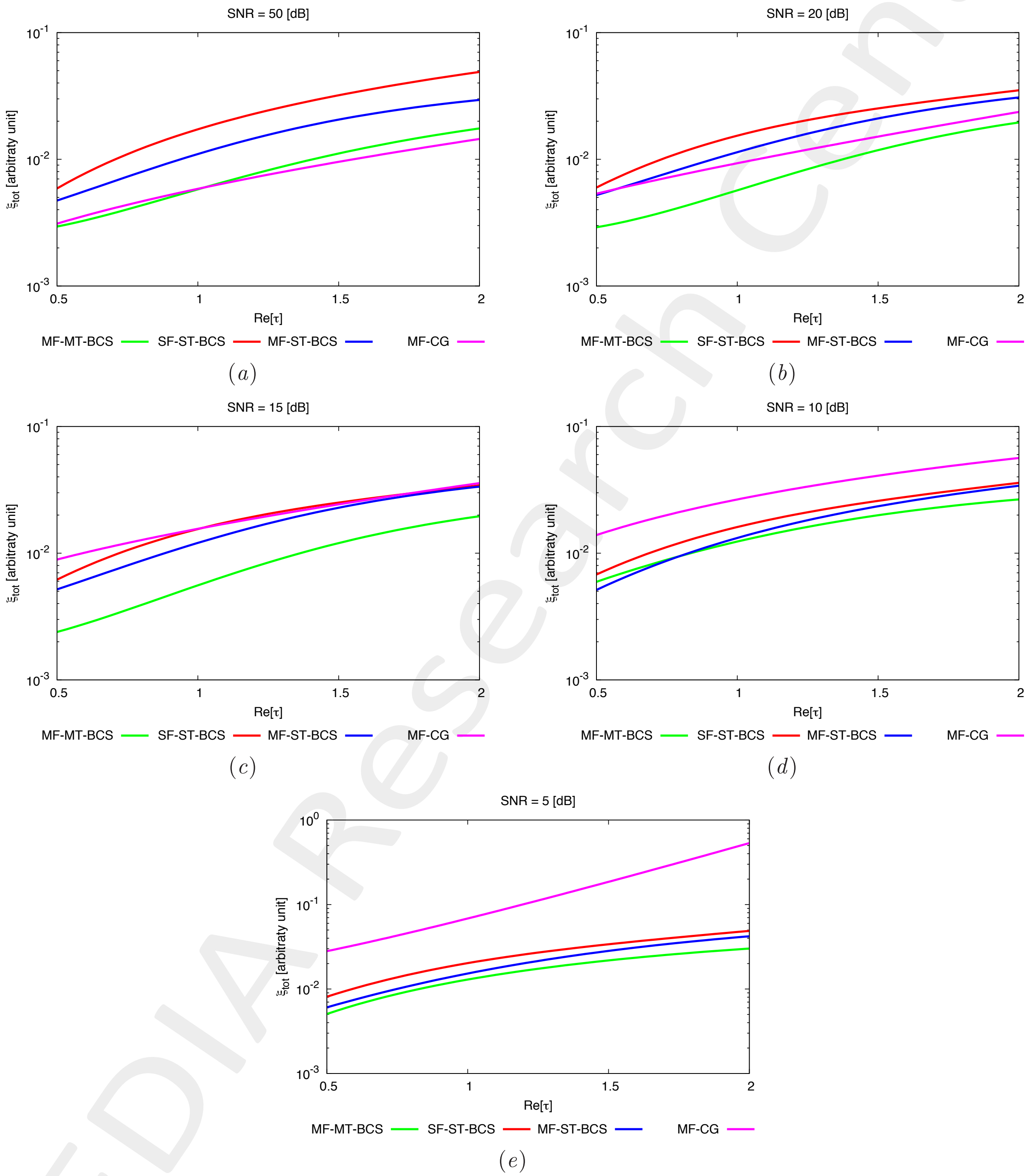

Figure 105. Behaviour of total error ξ_{tot} as a function of ε_r, for $SNR = 50$ [dB] (a), $SNR = 20$ [dB] (b), $SNR = 15$ [dB] (c), $SNR = 10$ [dB] (d) and $SNR = 5$ [dB] (e).

Homogeneous Rectangle of Sides $l_1 = 0.66\lambda$, $l_2 = 0.33\lambda$ - BCS/CG Errors vs. SNR Comparison

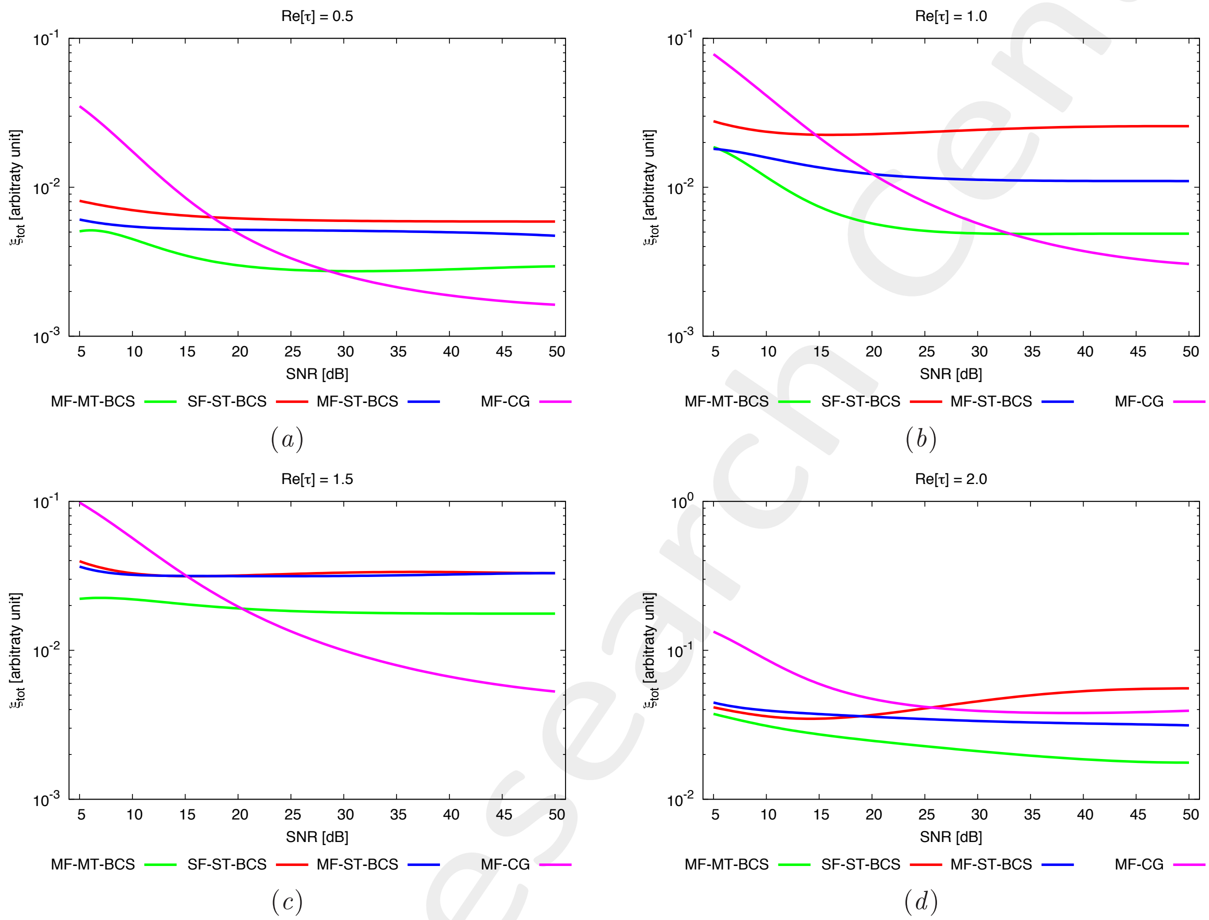

Figure 106. Behaviour of total error ξ_{tot} as a function of SNR, for $\varepsilon_r = 1.5$ [dB] (a), $\varepsilon_r = 2.0$ [dB] (b), $\varepsilon_r = 2.5$ [dB] (c) and $\varepsilon_r = 3.0$ [dB] (d).

0.2 Non-Homogeneous Objects

0.2.1 Three Objects Different Shapes

Goal: show the performances of the multi-frequency $MT-BCS$ when dealing with a sparse scatterer

- Number of frequencies F
- Number of Views: V
- Number of Measurements: M
- Number of Cells for the Inversion: N
- Number of Cells for the Direct solver: D
- Side of the investigation domain: L

Test Case Description

Direct solver:

- Square domain divided in $\sqrt{D} \times \sqrt{D}$ cells
- Domain side: $L = 3\lambda$ (at the central frequency)
- $D = 1296$ (discretization for the direct solver: $< \lambda/10$)

Investigation domain:

- Square domain divided in $\sqrt{N} \times \sqrt{N}$ cells
- $L = 3\lambda$
- $2ka = 2 \times \frac{2\pi}{\lambda} \times \frac{L\sqrt{2}}{2} = 6\pi\sqrt{2} = 26.65$
- $\#DOF = \frac{(2ka)^2}{2} = \frac{(2\times\frac{2\pi}{\lambda}\times\frac{L\sqrt{2}}{2})^2}{2} = 4\pi^2\left(\frac{L}{\lambda}\right)^2 = 4\pi^2 \times 9 \approx 355.3$
- N scelto in modo da essere vicino a $\#DOF$: $N = 324$ (18×18)

Measurement domain:

- Measurement points taken on a circle of radius $\rho = 3\lambda$ (at the central frequency)
- $M \approx 2ka \rightarrow M = 27$

Sources:

- $V = 1$ $(\theta = 0°)$
- Amplitude: $A = 1$ (plane waves)
- Number of Frequencies: $F = 11$
- Frequency Range: $I_F = [150\,Mhz\,:\,450MHz]$ - Frequency Step: $S_F = [30\,Mhz]$

Object:

- Strip of sides $l_1^{obj_1} = 0.16\lambda$, $l_2^{obj_1} = 0.50\lambda$; Square cylinder of side $l^{obj_2} = 0.33\lambda$; L-shaped cylinder
- $\varepsilon_r^{obj_1} = 1.6$; $\varepsilon_r^{obj_2} = \in \{1.5, 2.0, 2.5, 3.0, 3.5, 4.0, 4.5, 5.0\}$; $\varepsilon_r^{obj_3} = 2.4$
- $\sigma = 0$ [S/m]

BCS parameters:

- Gamma prior on noise variance parameters: $\beta_1 = 6.5 \times 10^{-1}$, $\beta_2 = 5.8 \times 10^{-2}$
- Convergenze parameter: $\tau = 1.0 \times 10^{-8}$

Three Non-Homogeneous Objects of Different Shapes - $\varepsilon_r = 1.5$ - BCS/CG Reconstructions Comparison

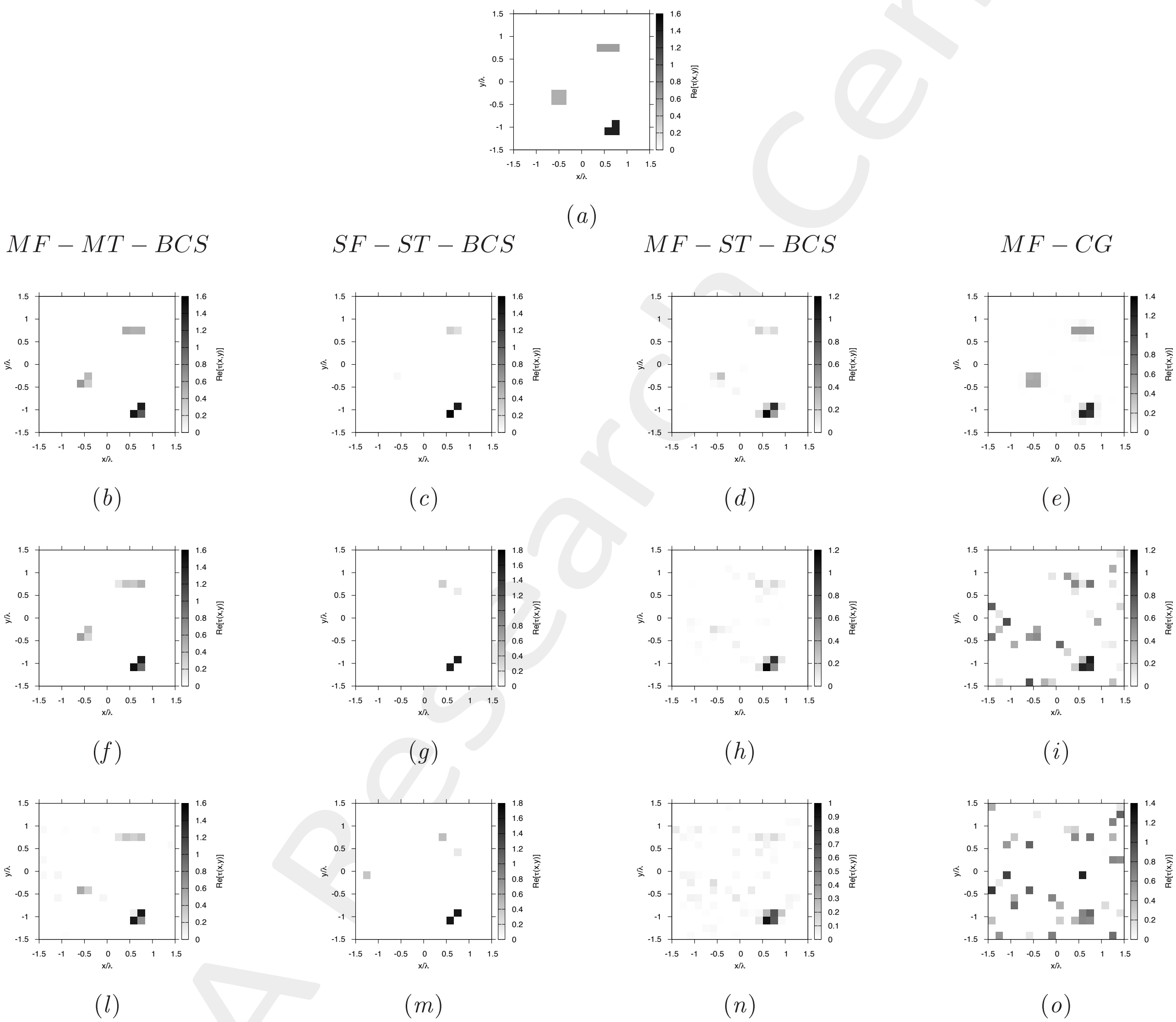

Figure 107. Actual object (a), $MF-MT-BCS$ $(b)(f)(l)$, $SF-ST-BCS$ $(c)(g)(m)$,$MF-ST-BCS$ $(d)(h)(n)$ and $MF-CG$ $(e)(i)(o)$ reconstructed object for $SNR = 50$ [dB] $(b)(c)(d)(e)$, $SNR = 10$ [dB] $(f)(g)(h)(i)$ and $SNR = 5$ [dB] $(l)(m)(n)(o)$.

Three Non-Homogeneous Objects of Different Shapes - $\varepsilon_r = 2.0$ - BCS/CG Reconstructions Comparison

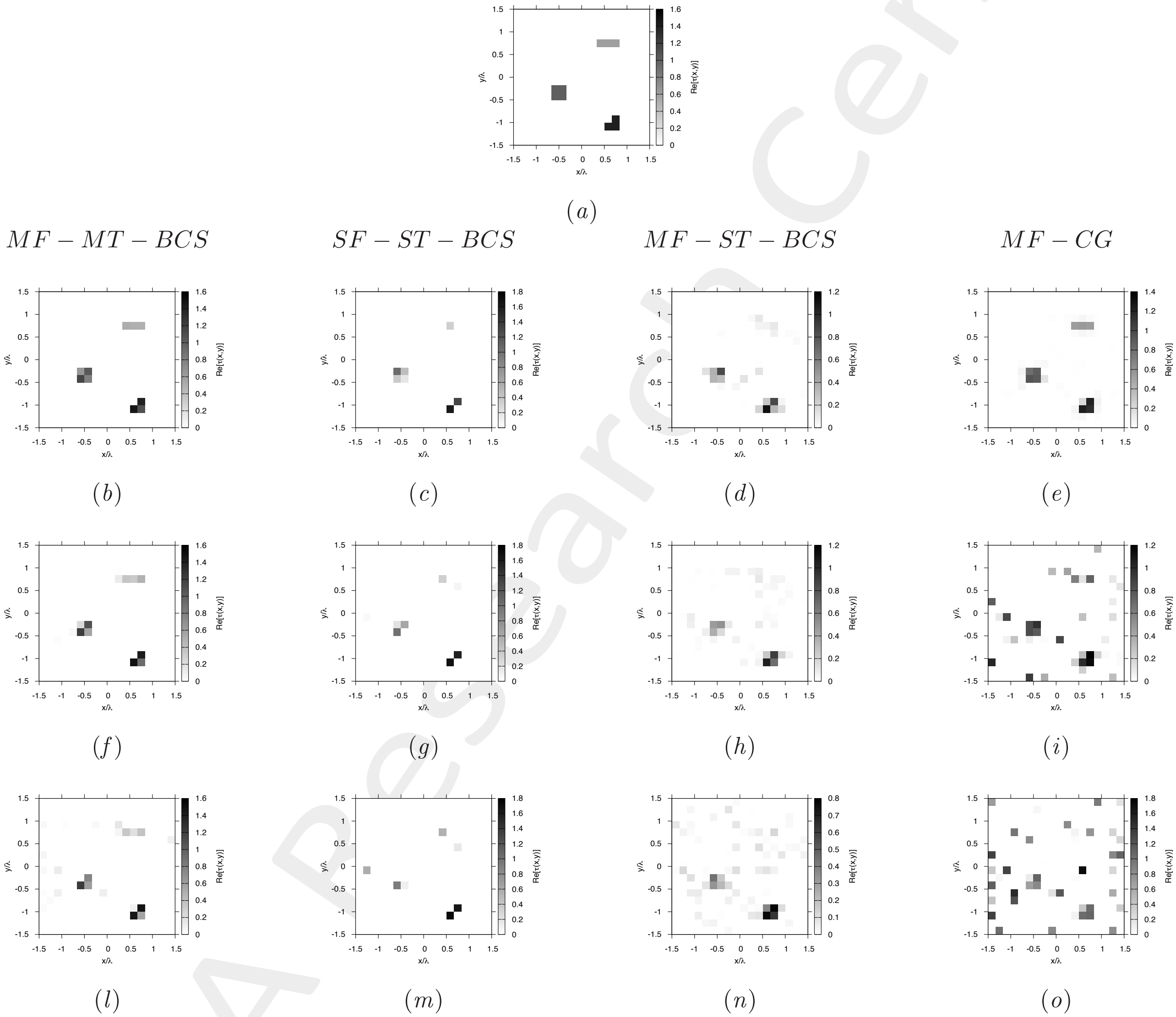

Figure 108. Actual object (a), $MF-MT-BCS$ $(b)(f)(l)$, $SF-ST-BCS$ $(c)(g)(m)$,$MF-ST-BCS$ $(d)(h)(n)$ and $MF-CG$ $(e)(i)(o)$ reconstructed object for $SNR = 50$ [dB] $(b)(c)(d)(e)$, $SNR = 10$ [dB] $(f)(g)(h)(i)$ and $SNR = 5$ [dB] $(l)(m)(n)(o)$.

Three Non-Homogeneous Objects of Different Shapes - $\varepsilon_r = 3.0$ - BCS/CG Reconstructions Comparison

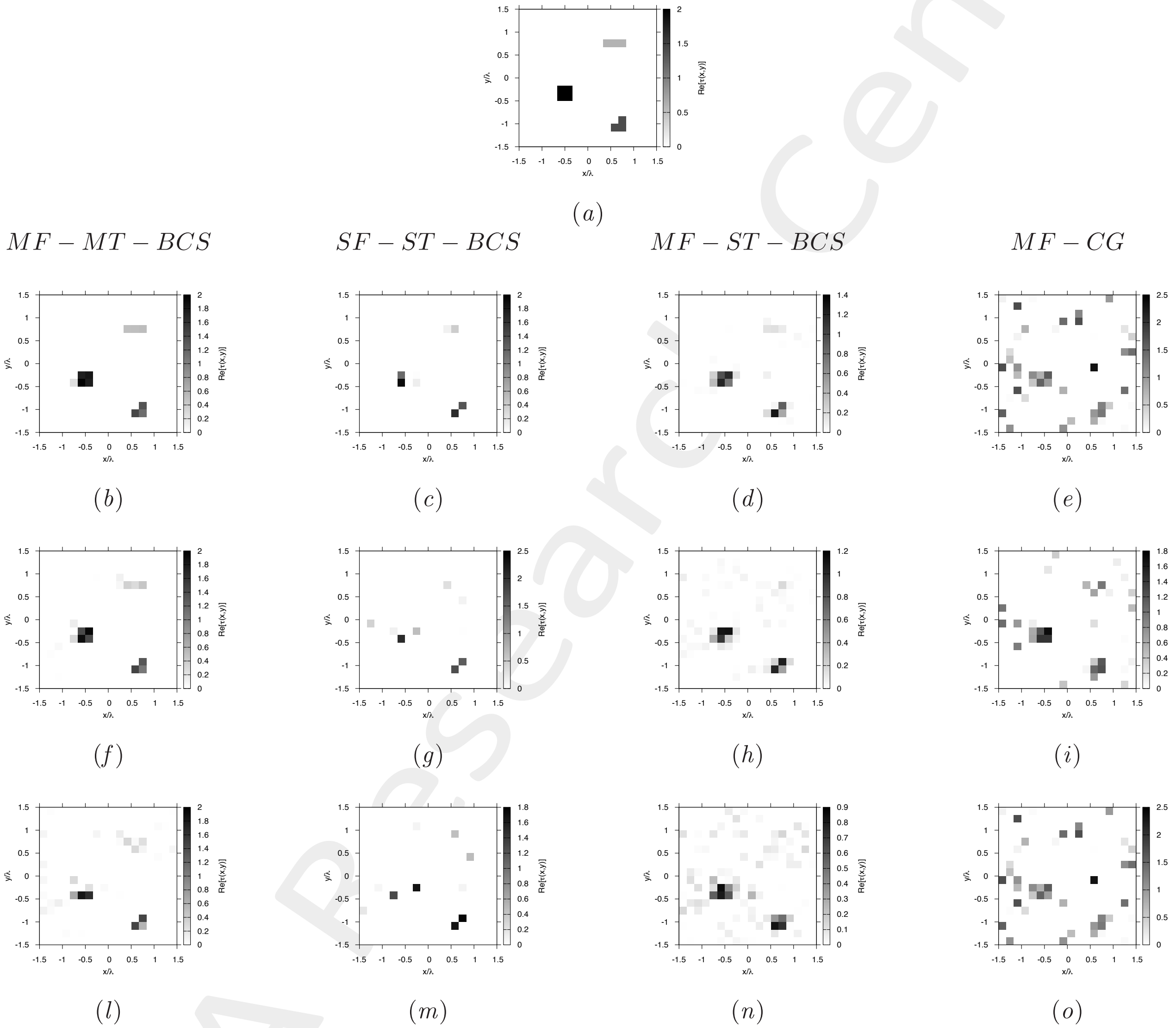

Figure 109. Actual object (a), $MF-MT-BCS$ $(b)(f)(l)$, $SF-ST-BCS$ $(c)(g)(m)$,$MF-ST-BCS$ $(d)(h)(n)$ and $MF-CG$ $(e)(i)(o)$ reconstructed object for $SNR = 50$ [dB] $(b)(c)(d)(e)$, $SNR = 10$ [dB] $(f)(g)(h)(i)$ and $SNR = 5$ [dB] $(l)(m)(n)(o)$.

Three Non-Homogeneous Objects of Different Shapes - $\varepsilon_r = 4.0$ - BCS/CG Reconstructions Comparison

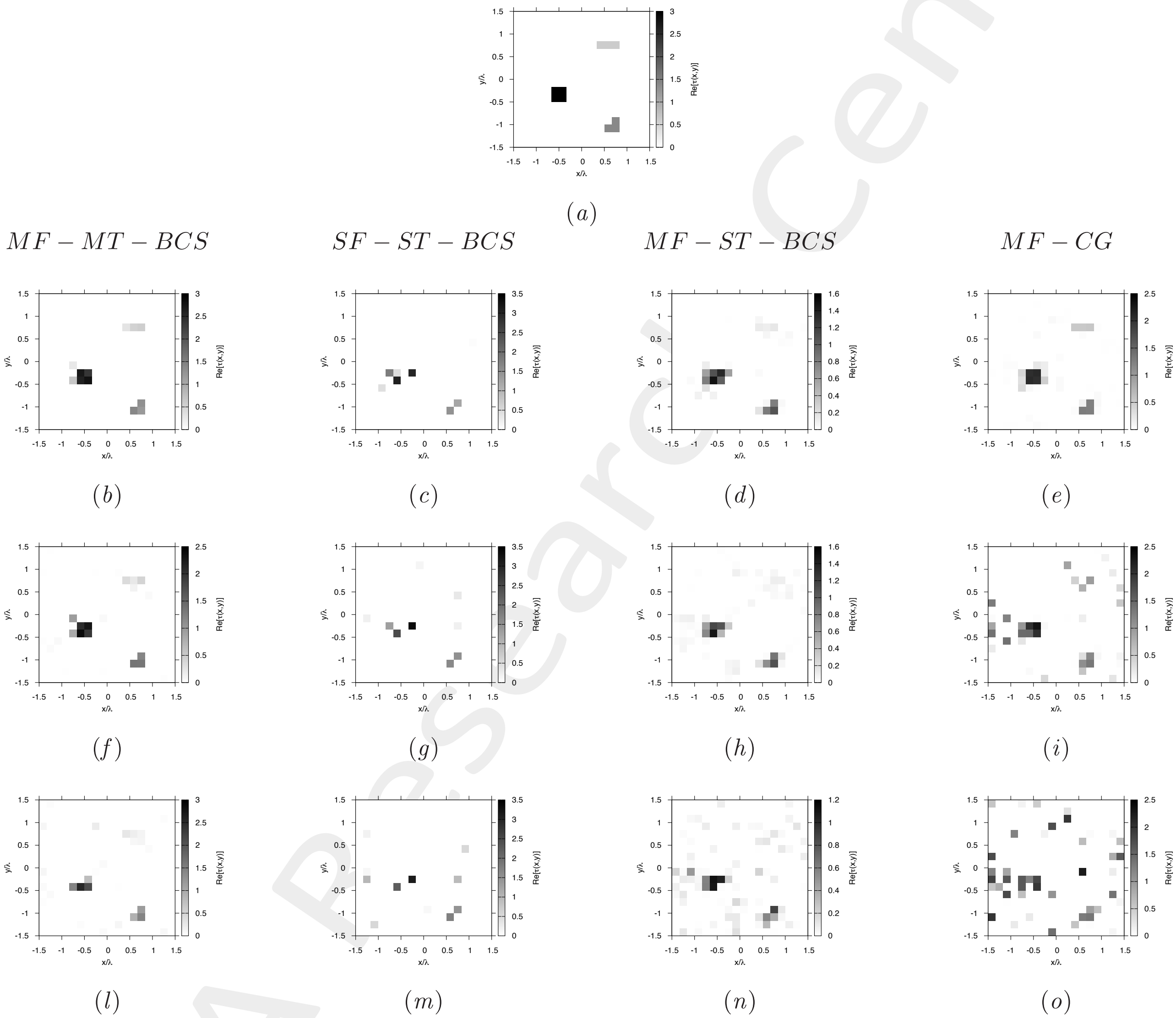

Figure 110. Actual object (a), $MF - MT - BCS$ $(b)(f)(l)$, $SF - ST - BCS$ $(c)(g)(m)$,$MF - ST - BCS$ $(d)(h)(n)$ and $MF - CG$ $(e)(i)(o)$ reconstructed object for $SNR = 50$ [dB] $(b)(c)(d)(e)$, $SNR = 10$ [dB] $(f)(g)(h)(i)$ and $SNR = 5$ [dB] $(l)(m)(n)(o)$.

Three Non-Homogeneous Objects of Different Shapes - $\varepsilon_r = 5.0$ - BCS/CG Reconstructions Comparison

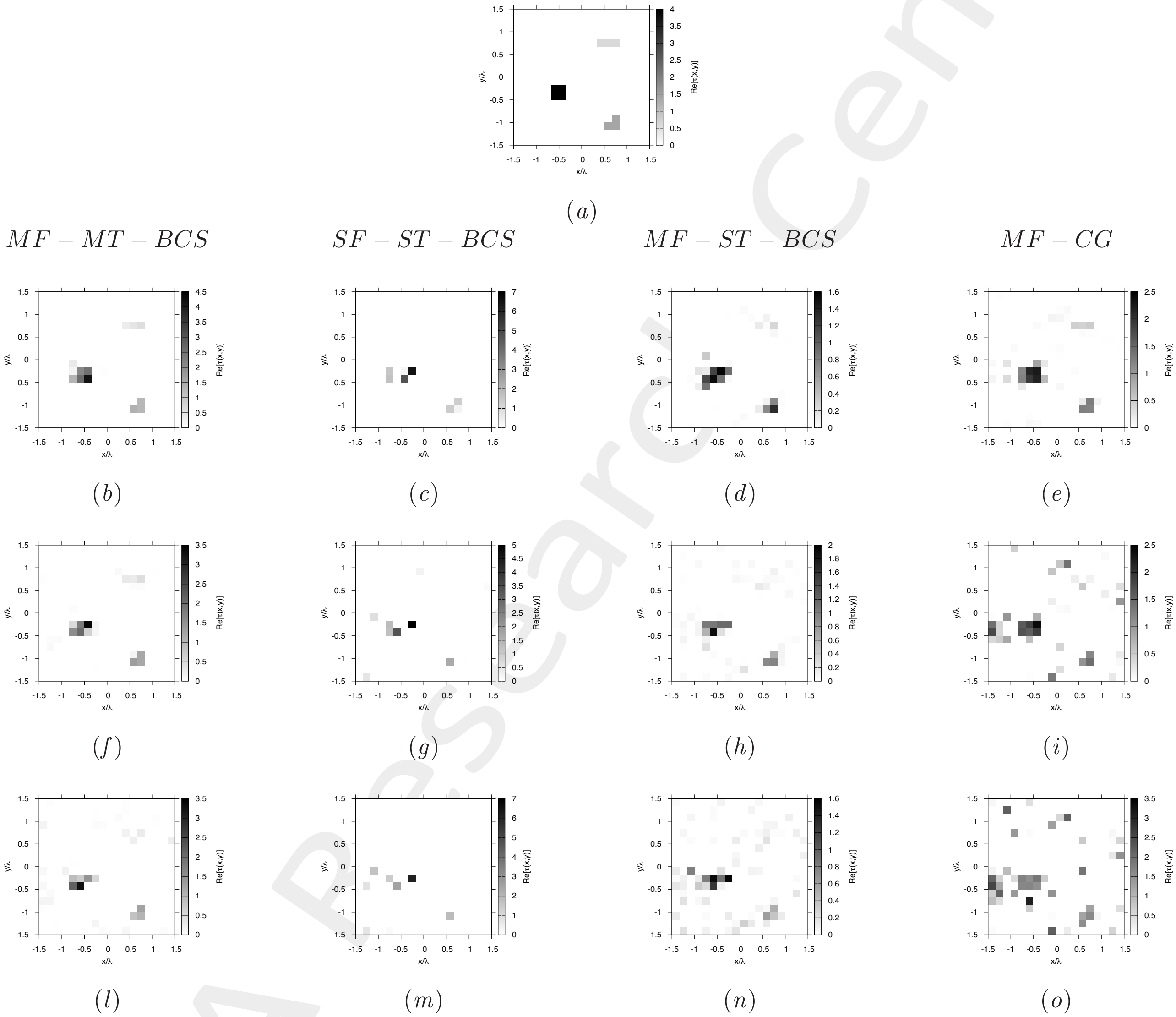

Figure 111. Actual object (a), $MF - MT - BCS$ $(b)(f)(l)$, $SF - ST - BCS$ $(c)(g)(m)$,$MF - ST - BCS$ $(d)(h)(n)$ and $MF - CG$ $(e)(i)(o)$ reconstructed object for $SNR = 50$ [dB] $(b)(c)(d)(e)$, $SNR = 10$ [dB] $(f)(g)(h)(i)$ and $SNR = 5$ [dB] $(l)(m)(n)(o)$.

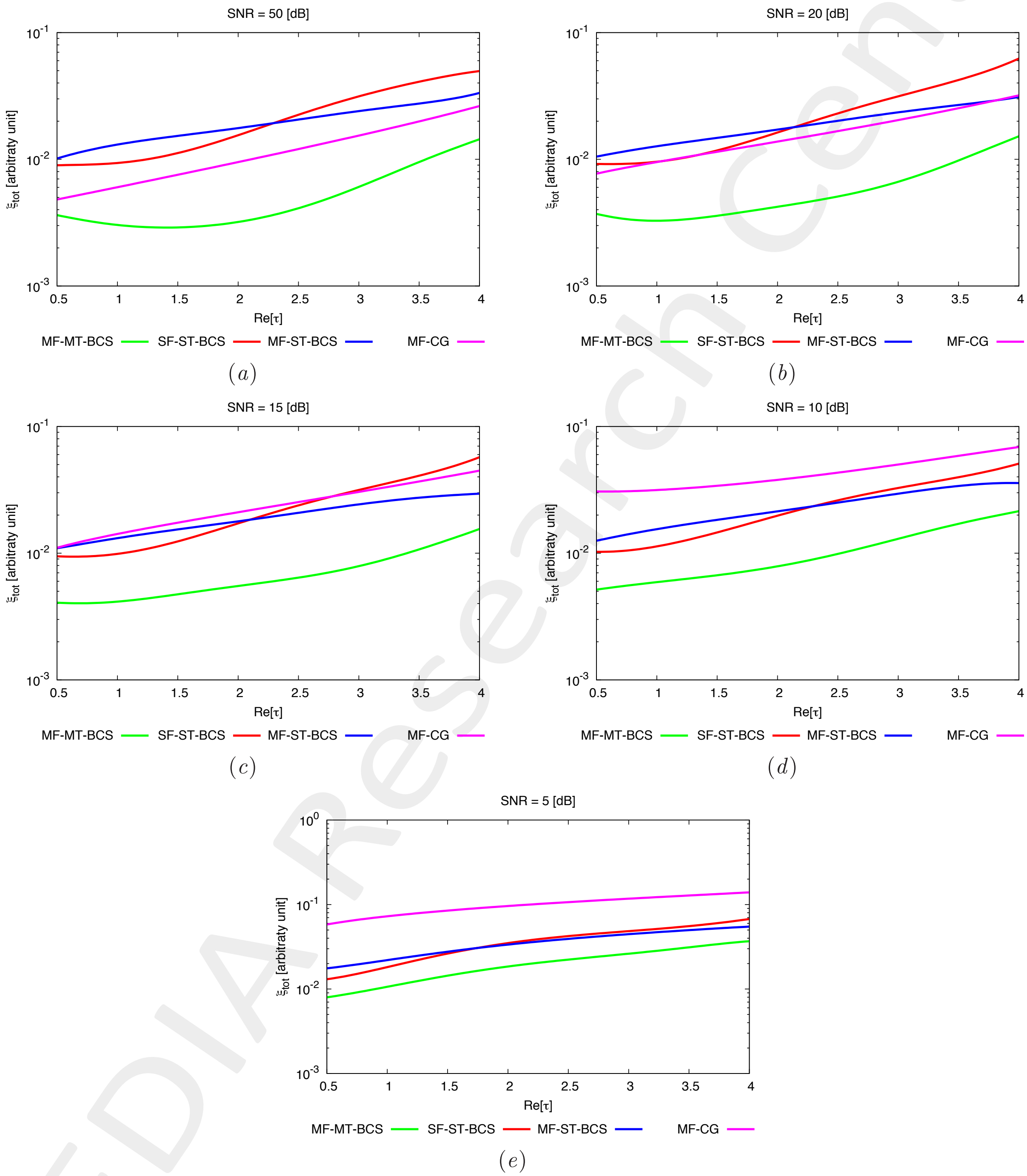

Figure 112. Behaviour of total error ξ_{tot} as a function of ε_r, for $SNR = 50$ [dB] (a), $SNR = 20$ [dB] (b), $SNR = 15$ [dB] (c), $SNR = 10$ [dB] (d) and $SNR = 5$ [dB] (e).

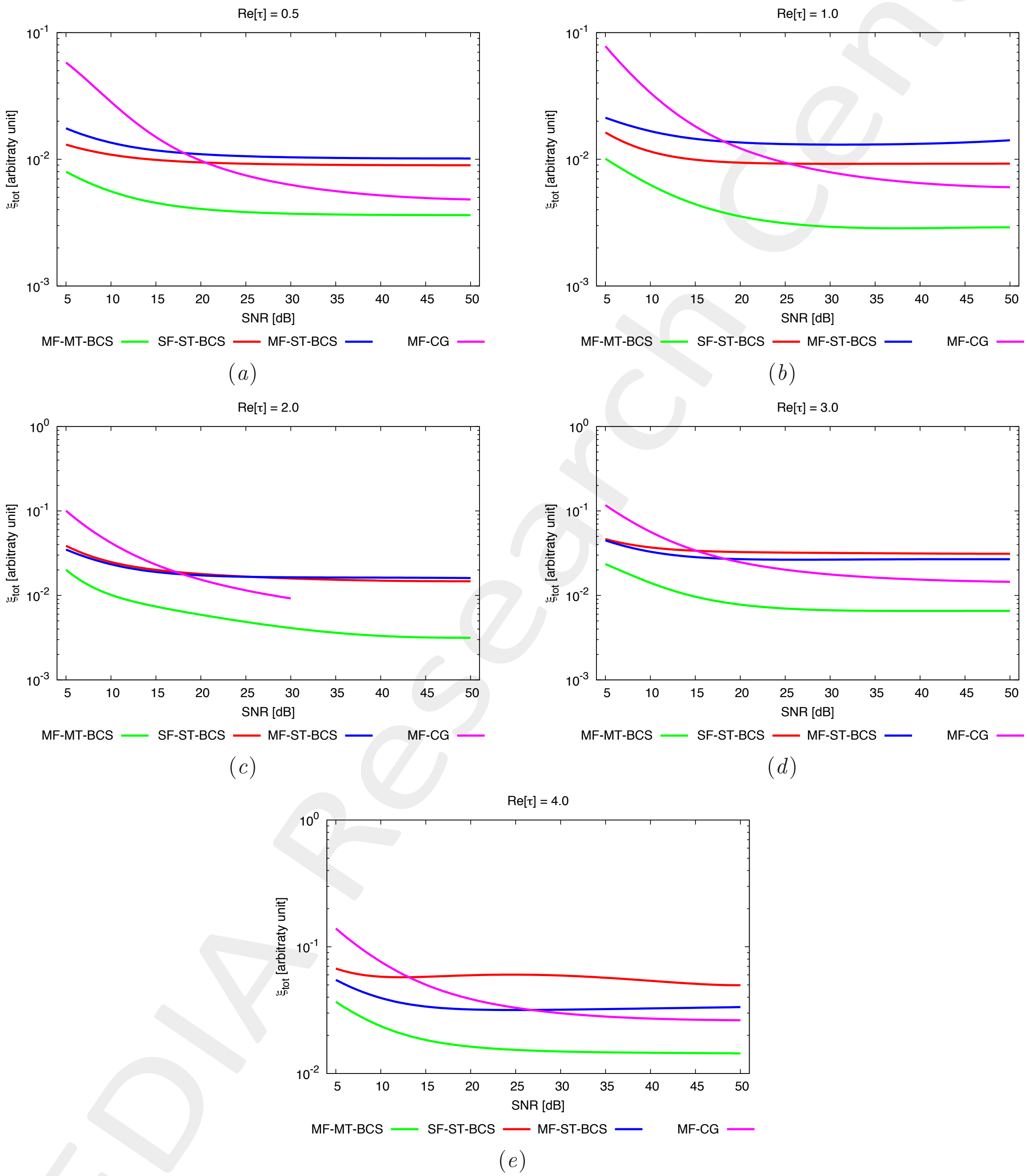

Figure 113. Behaviour of total error ξ_{tot} as a function of SNR, for $\varepsilon_r = 1.5$ [dB] (a), $\varepsilon_r = 2.0$ [dB] (b), $\varepsilon_r = 3.0$ [dB] (c), $\varepsilon_r = 4.0$ [dB] (d) and $\varepsilon_r = 5.0$ [dB] (e).

0.2.2 Rectangle of Sides $l_1 = 0.66\lambda$, $l_2 = 0.33\lambda$ and Square of Side $l_3 = 0.33\lambda$

Goal: show the performances of the multi-frequency $MT - BCS$ when dealing with a sparse scatterer

- Number of frequencies F
- Number of Views: V
- Number of Measurements: M
- Number of Cells for the Inversion: N
- Number of Cells for the Direct solver: D
- Side of the investigation domain: L

Test Case Description

Direct solver:

- Square domain divided in $\sqrt{D} \times \sqrt{D}$ cells
- Domain side: $L = 3\lambda$ (at the central frequency)
- $D = 1296$ (discretization for the direct solver: $< \lambda/10$)

Investigation domain:

- Square domain divided in $\sqrt{N} \times \sqrt{N}$ cells
- $L = 3\lambda$
- $2ka = 2 \times \frac{2\pi}{\lambda} \times \frac{L\sqrt{2}}{2} = 6\pi\sqrt{2} = 26.65$
- $\#DOF = \frac{(2ka)^2}{2} = \frac{(2\times\frac{2\pi}{\lambda}\times\frac{L\sqrt{2}}{2})^2}{2} = 4\pi^2\left(\frac{L}{\lambda}\right)^2 = 4\pi^2 \times 9 \approx 355.3$
- N scelto in modo da essere vicino a $\#DOF$: $N = 324$ (18×18)

Measurement domain:

- Measurement points taken on a circle of radius $\rho = 3\lambda$ (at the central frequency)
- $M \approx 2ka \rightarrow M = 27$

Sources:

- $V = 1$ $(\theta = 0°)$
- Amplitude: $A = 1$ (plane waves)
- Number of Frequencies: $F = 11$
- Frequency Range: $I_F = [150\,Mhz : 450MHz]$ - Frequency Step: $S_F = [30\,Mhz]$

Object:

- Rectangle of sides $l_1^{obj_1} = 0.33\lambda$, $l_2^{obj_1} = 0.66\lambda$; Square of sides $l^{obj_2} = 0.33\lambda$
- $\varepsilon_r^{obj_1} = 1.9$, $\varepsilon_r^{obj_2} \in \{1.5, 2.0, 2.5, 3.0, 3.5, 4.0, 4.5, 5.0\}$
- $\sigma = 0$ [S/m]

BCS parameters:

- Gamma prior on noise variance parameters: $\beta_1 = 6.5 \times 10^{-1}$, $\beta_2 = 5.8 \times 10^{-2}$
- Convergenze parameter: $\tau = 1.0 \times 10^{-8}$

Non-Homogeneous Rectangle of Sides $l_1^{obj_1} = 0.66\lambda$, $l_2^{obj_1} = 0.33\lambda$ and Square of Side $l^{obj_2} = 0.33\lambda$ - BCS/CG Reconstructions Comparison

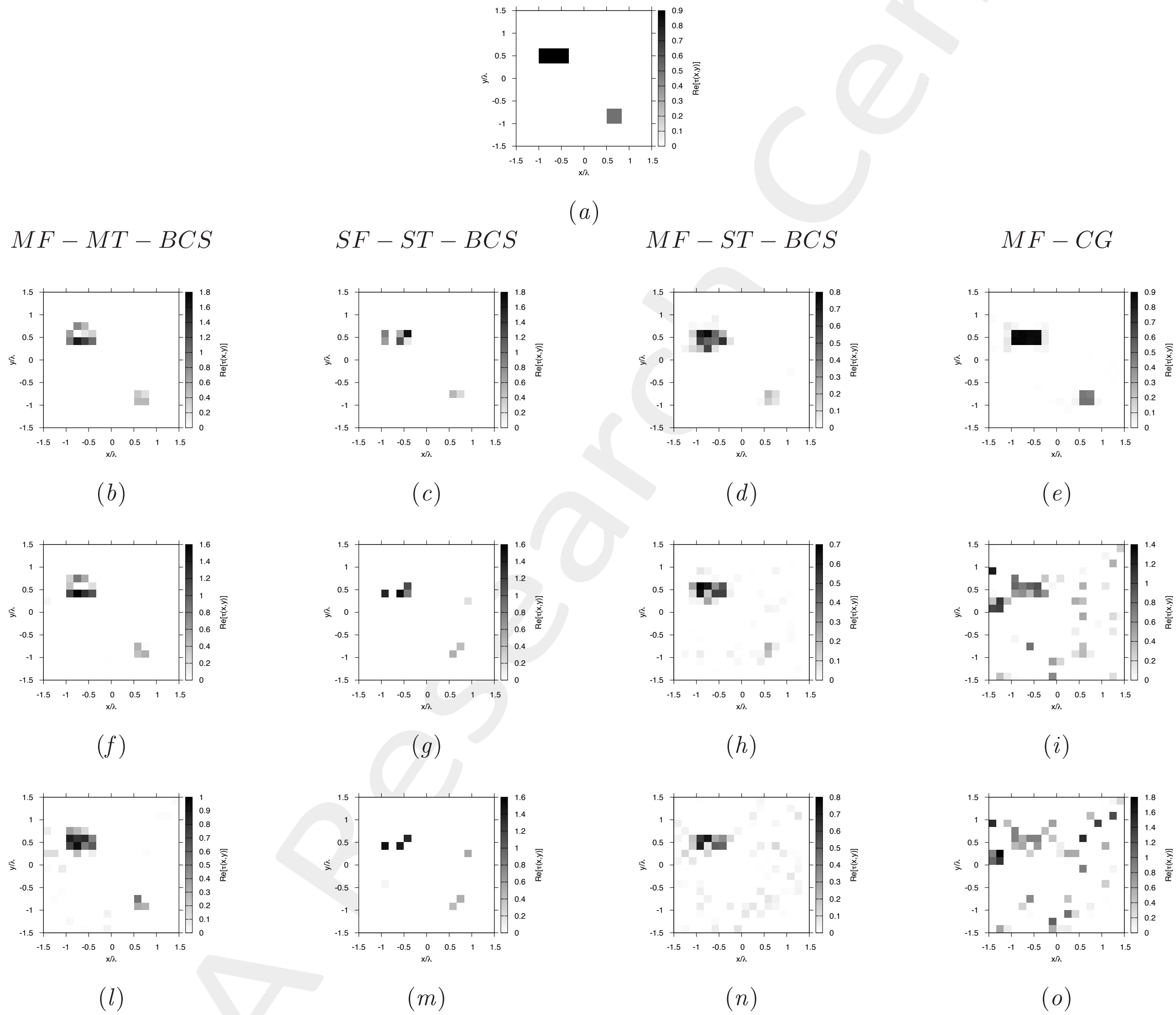

Figure 114. Actual object (a), $MF-MT-BCS$ $(b)(f)(l)$, $SF-ST-BCS$ $(c)(g)(m)$,$MF-ST-BCS$ $(d)(h)(n)$ and $MF-CG$ $(e)(i)(o)$ reconstructed object for $SNR = 50$ [dB] $(b)(c)(d)(e)$, $SNR = 10$ [dB] $(f)(g)(h)(i)$ and $SNR = 5$ [dB] $(l)(m)(n)(o)$.

Non-Homogeneous Rectangle of Sides $l_1^{obj_1} = 0.66\lambda$, $l_2^{obj_1} = 0.33\lambda$ and Square of Side $l^{obj_2} = 0.33\lambda$ - BCS/CG Reconstructions Comparison

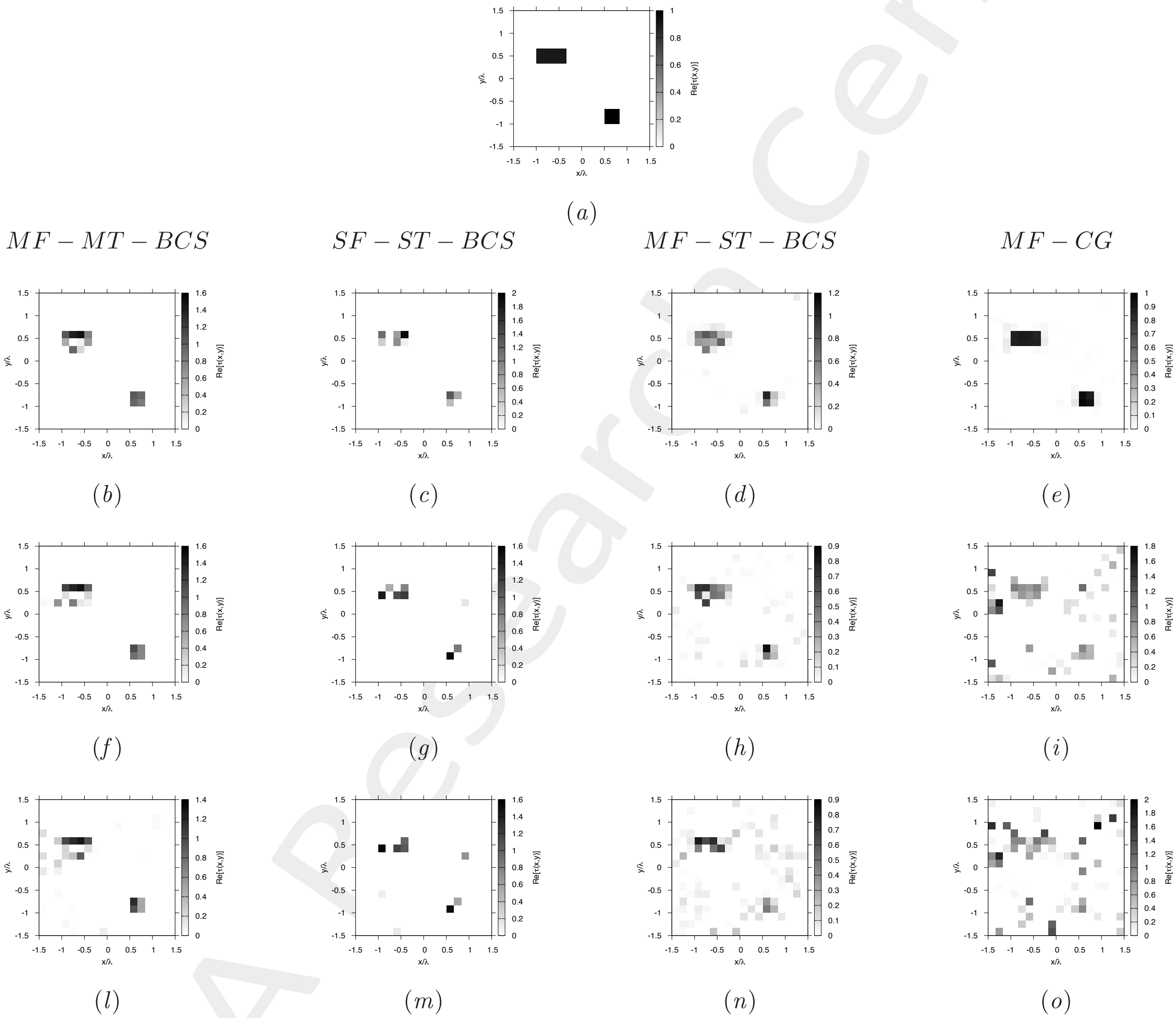

Figure 115. Actual object (a), $MF-MT-BCS$ $(b)(f)(l)$, $SF-ST-BCS$ $(c)(g)(m)$,$MF-ST-BCS$ $(d)(h)(n)$ and $MF-CG$ $(e)(i)(o)$ reconstructed object for $SNR = 50$ [dB] $(b)(c)(d)(e)$, $SNR = 10$ [dB] $(f)(g)(h)(i)$ and $SNR = 5$ [dB] $(l)(m)(n)(o)$.

Non-Homogeneous Rectangle of Sides $l_1^{obj_1} = 0.66\lambda$, $l_2^{obj_1} = 0.33\lambda$ and Square of Side $l^{obj_2} = 0.33\lambda$ - BCS/CG Reconstructions Comparison

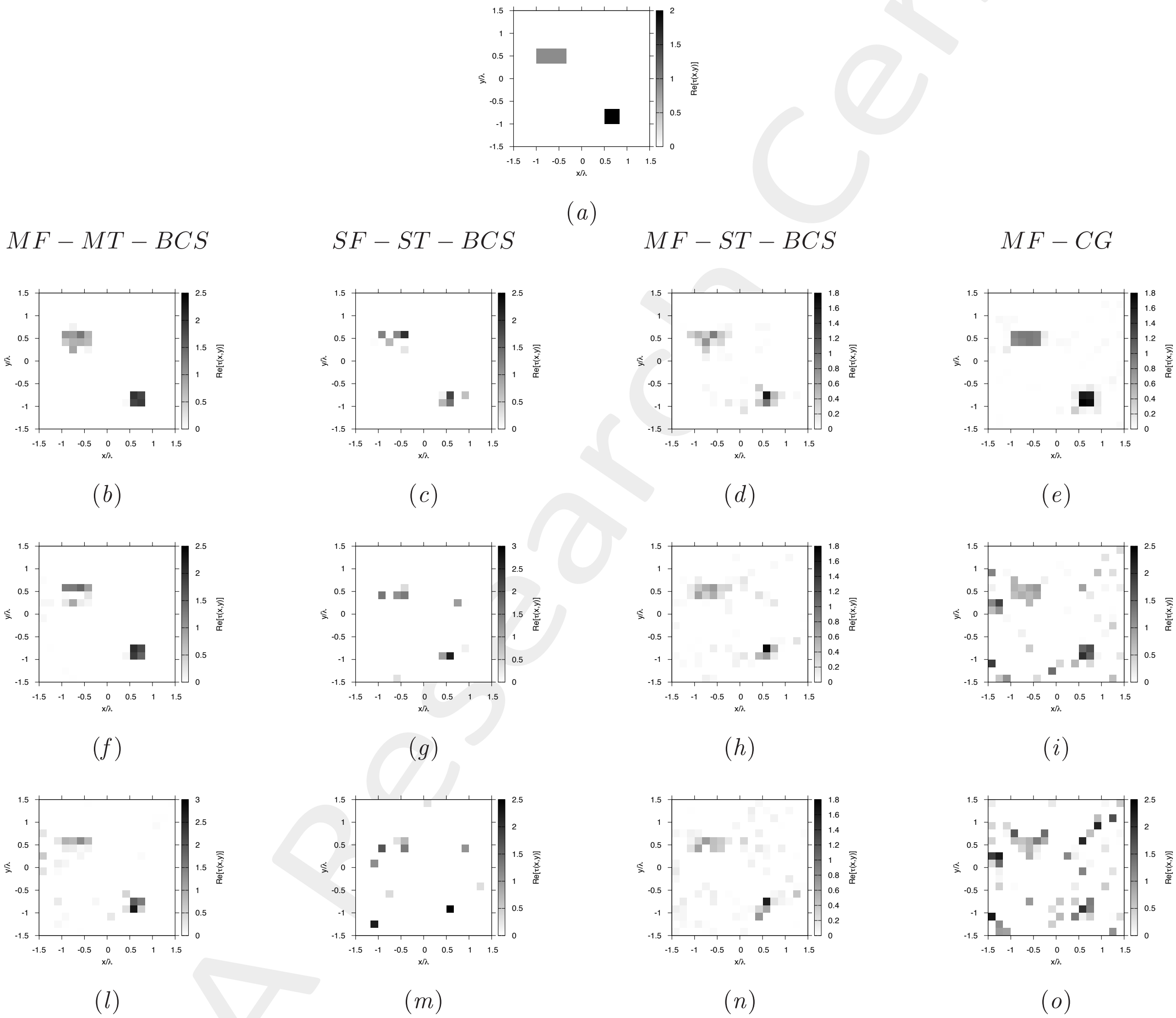

(a)

$MF - MT - BCS$ $SF - ST - BCS$ $MF - ST - BCS$ $MF - CG$

(b) (c) (d) (e)

(f) (g) (h) (i)

(l) (m) (n) (o)

Figure 116. Actual object (a), $MF-MT-BCS$ $(b)(f)(l)$, $SF-ST-BCS$ $(c)(g)(m)$,$MF-ST-BCS$ $(d)(h)(n)$ and $MF-CG$ $(e)(i)(o)$ reconstructed object for $SNR = 50$ [dB] $(b)(c)(d)(e)$, $SNR = 10$ [dB] $(f)(g)(h)(i)$ and $SNR = 5$ [dB] $(l)(m)(n)(o)$.

Non-Homogeneous Rectangle of Sides $l_1^{obj_1} = 0.66\lambda$, $l_2^{obj_1} = 0.33\lambda$ and Square of Side $l^{obj_2} = 0.33\lambda$ - BCS/CG Reconstructions Comparison

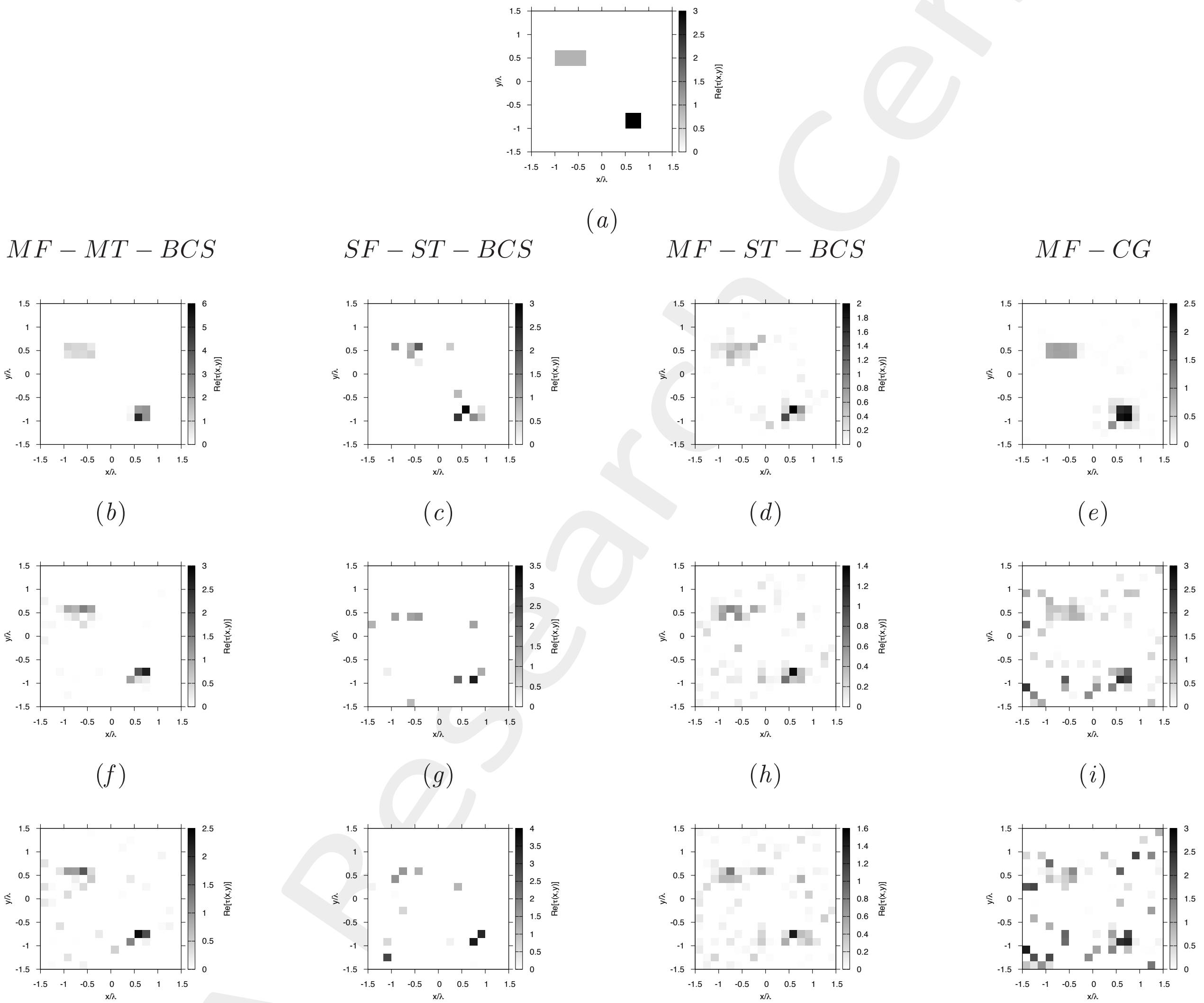

(a)

$MF - MT - BCS$ $SF - ST - BCS$ $MF - ST - BCS$ $MF - CG$

(b) (c) (d) (e)

(f) (g) (h) (i)

(l) (m) (n) (o)

Figure 117. Actual object (a), $MF - MT - BCS$ $(b)(f)(l)$, $SF - ST - BCS$ $(c)(g)(m)$,$MF - ST - BCS$ $(d)(h)(n)$ and $MF - CG$ $(e)(i)(o)$ reconstructed object for $SNR = 50$ [dB] $(b)(c)(d)(e)$, $SNR = 10$ [dB] $(f)(g)(h)(i)$ and $SNR = 5$ [dB] $(l)(m)(n)(o)$.

Non-Homogeneous Rectangle of Sides $l_1^{obj_1} = 0.66\lambda$, $l_2^{obj_1} = 0.33\lambda$ and Square of Side $l^{obj_2} = 0.33\lambda$ - BCS/CG Reconstructions Comparison

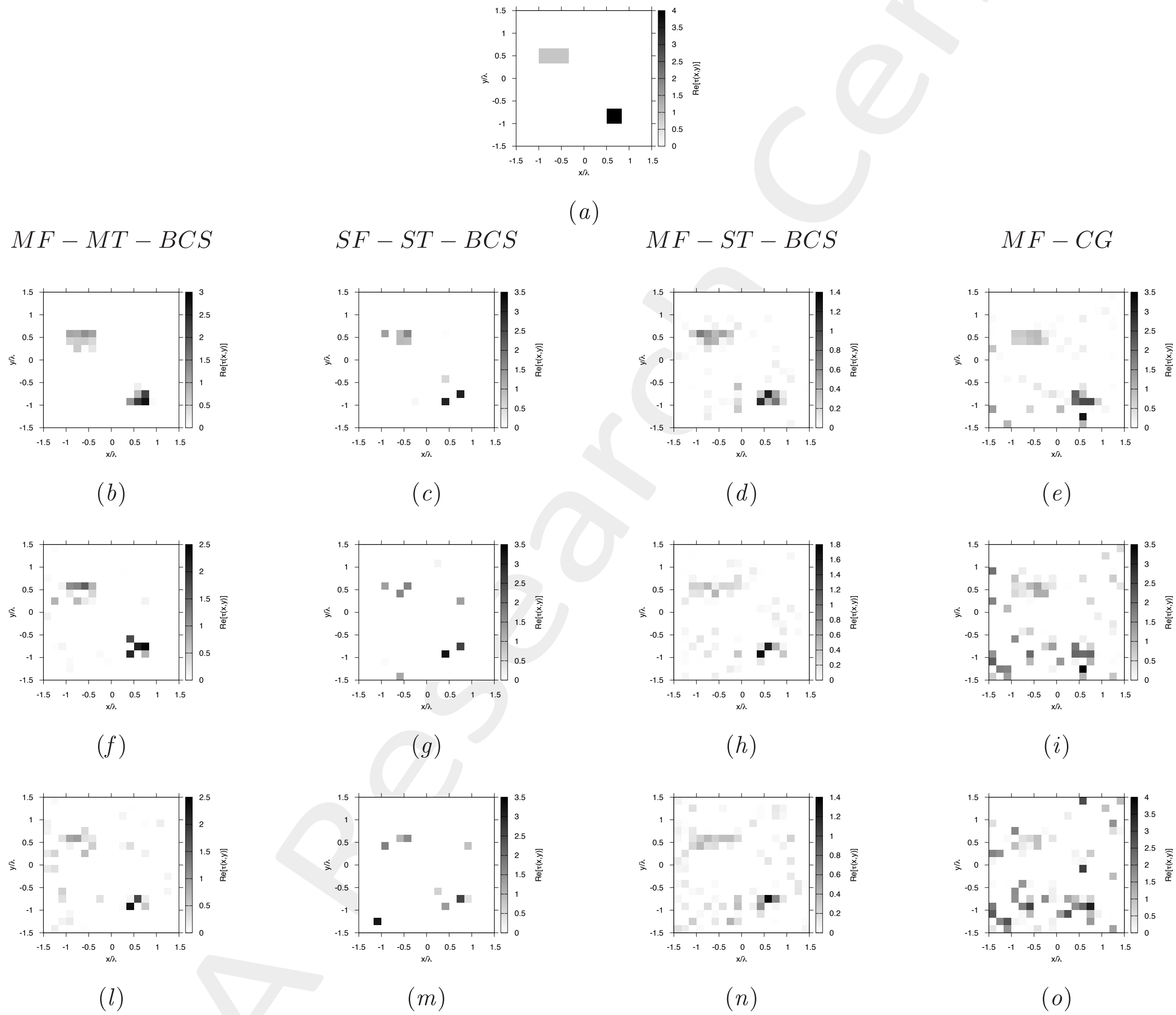

Figure 118. Actual object (a), $MF-MT-BCS$ $(b)(f)(l)$, $SF-ST-BCS$ $(c)(g)(m)$,$MF-ST-BCS$ $(d)(h)(n)$ and $MF-CG$ $(e)(i)(o)$ reconstructed object for $SNR = 50$ [dB] $(b)(c)(d)(e)$, $SNR = 10$ [dB] $(f)(g)(h)(i)$ and $SNR = 5$ [dB] $(l)(m)(n)(o)$.

Non-Homogeneous Rectangle of Sides $l_1^{obj_1} = 0.66\lambda$, $l_2^{obj_1} = 0.33\lambda$ and Square of Side $l^{obj_2} = 0.33\lambda$ - BCS/CG Errors vs. ε_r Comparison

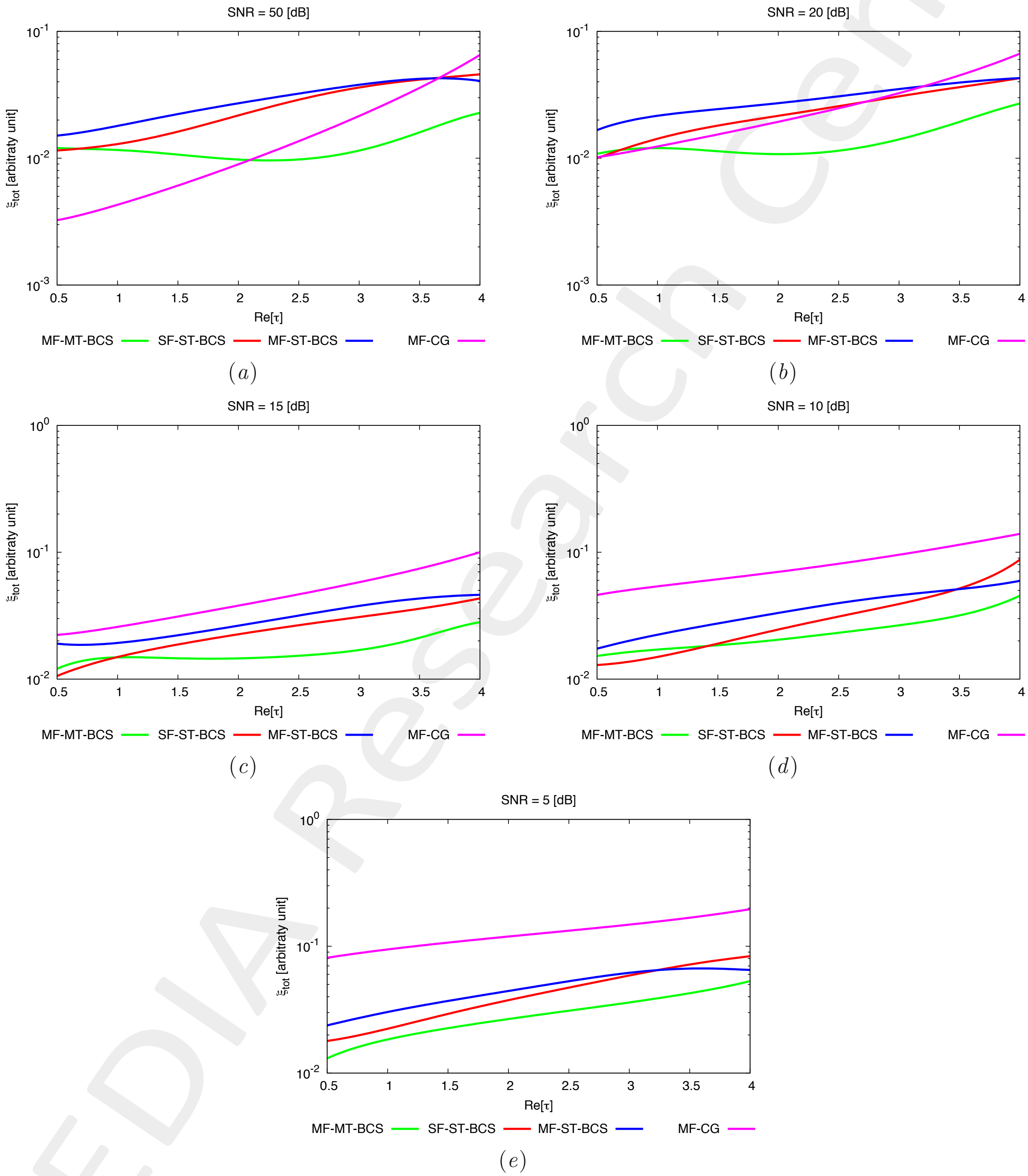

Figure 119. Behaviour of total error ξ_{tot} as a function of ε_r, for $SNR = 50$ [dB] (a), $SNR = 20$ [dB] (b), $SNR = 15$ [dB] (c), $SNR = 10$ [dB] (d) and $SNR = 5$ [dB] (e).

Non-Homogeneous Rectangle of Sides $l_1^{obj_1} = 0.66\lambda$, $l_2^{obj_1} = 0.33\lambda$ and Square of Side $l^{obj_2} = 0.33\lambda$ - BCS/CG Errors vs. ε_r Comparison

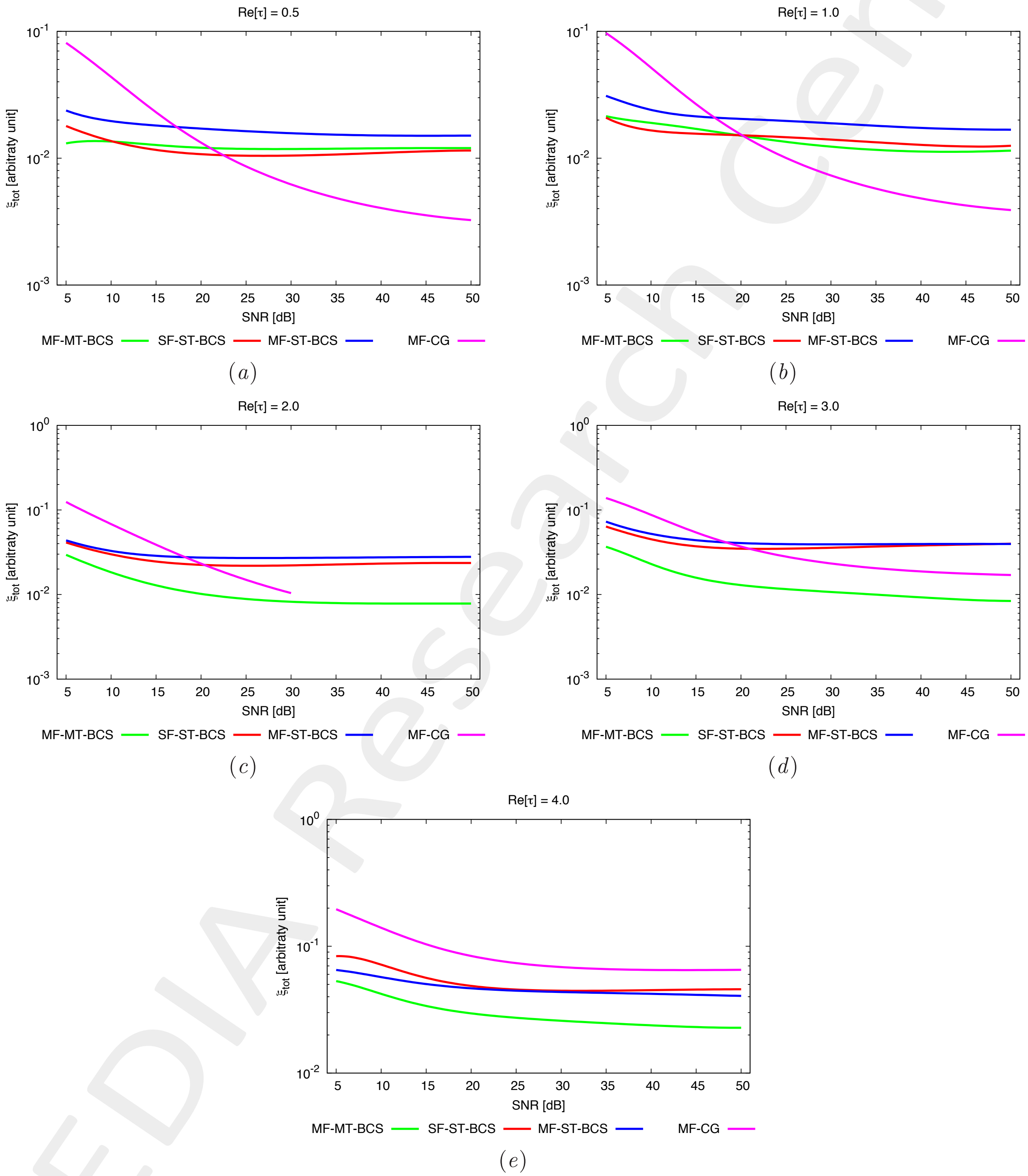

Figure 120. Behaviour of total error ξ_{tot} as a function of SNR, for $\varepsilon_r = 1.5$ [dB] (a), $\varepsilon_r = 2.0$ [dB] (b), $\varepsilon_r = 3.0$ [dB] (c), $\varepsilon_r = 4.0$ [dB] (d) and $\varepsilon_r = 5.0$ [dB] (e).

References

[1] G. Oliveri, P. Rocca, and A. Massa, "A Bayesian compressive sampling-based inversion for imaging sparse scatterers," IEEE Trans. Geosci. Remote Sens., vol. 49, no. 10, pp. 3993-4006, Oct. 2011.

[2] L. Poli, G. Oliveri, P.-P. Ding, T. Moriyama, and A. Massa, "Multifrequency Bayesian compressive sensing methods for microwave imaging," Journal of the Optical Society of the America A, vol. 31, no. 11, pp. 2415-2428, 2014.

[3] G. Oliveri, N. Anselmi, and A. Massa, "Compressive sensing imaging of non-sparse 2D scatterers by a total-variation approach within the Born approximation," IEEE Trans. Antennas Propag., vol. 62, no. 10, pp. 5157-5170, Oct. 2014.

[4] L. Poli, G. Oliveri, and A. Massa, "Imaging sparse metallic cylinders through a Local Shape Function Bayesian Compressive Sensing approach," Journal of Optical Society of America A, vol. 30, no. 6, pp. 1261-1272, 2013.

[5] F. Viani, L. Poli, G. Oliveri, F. Robol, and A. Massa, "Sparse scatterers imaging through approximated multitask compressive sensing strategies," Microwave Opt. Technol. Lett., vol. 55, no. 7, pp. 1553-1558, Jul. 2013.

[6] L. Poli, G. Oliveri, P. Rocca, and A. Massa, "Bayesian compressive sensing approaches for the reconstruction of two-dimensional sparse scatterers under TE illumination," IEEE Trans. Geosci. Remote Sensing, vol. 51, no. 5, pp. 2920-2936, May 2013.

[7] L. Poli, G. Oliveri, and A. Massa, "Microwave imaging within the first-order Born approximation by means of the contrast-field Bayesian compressive sensing," IEEE Trans. Antennas Propag., vol. 60, no. 6, pp. 2865-2879, Jun. 2012.

[8] G. Oliveri, L. Poli, P. Rocca, and A. Massa, "Bayesian compressive optical imaging within the Rytov approximation," Optics Letters, vol. 37, no. 10, pp. 1760-1762, 2012.

[9] L. Poli, G. Oliveri, F. Viani, and A. Massa, "MT-BCS-based microwave imaging approach through minimum-norm current expansion," IEEE Trans. Antennas Propag., vol. 61, no. 9, pp. 4722-4732, Sep. 2013.

[10] G. Oliveri, P.-P. Ding, and L. Poli "3D crack detection in anisotropic layered media through a sparseness-regularized solver," IEEE Antennas Wireless Propag. Lett., in press.

[11] M. Salucci, G. Oliveri, A. Randazzo, M. Pastorino, and A. Massa, "Electromagnetic subsurface prospecting by a multifocusing inexact Newton method within the second-order Born approximation," J. Opt. Soc. Am. A., vol. 31, no. 6, pp. 1167-1179, Jun. 2014.

[12] S. C. Hagness, E. C. Fear, and A. Massa, "Guest Editorial: Special Cluster on Microwave Medical Imaging," IEEE Antennas Wireless Propag. Lett., vol. 11, pp. 1592-1597, 2012.

[13] G. Oliveri, Y. Zhong, X. Chen, and A. Massa, "Multi-resolution subspace-based optimization method for inverse scattering," Journal of Optical Society of America A, vol. 28, no. 10, pp. 2057-2069, Oct. 2011.

[14] A. Randazzo, G. Oliveri, A. Massa, and M. Pastorino, "Electromagnetic inversion with the multiscaling inexact-Newton method - Experimental validation," Microwave Opt. Technol. Lett., vol. 53, no. 12, pp. 2834-2838, Dec. 2011.

[15] G. Oliveri, L. Lizzi, M. Pastorino, and A. Massa, "A nested multi-scaling inexact-Newton iterative approach for microwave imaging," IEEE Trans. Antennas Propag., vol. 60, no. 2, pp. 971-983, Feb. 2012.

[16] G. Oliveri, A. Randazzo, M. Pastorino, and A. Massa, "Electromagnetic imaging within the contrast-source formulation by means of the multiscaling inexact Newton method," Journal of Optical Society of America A, vol. 29, no. 6, pp. 945-958, 2012.

[17] M. Benedetti, D. Lesselier, M. Lambert, and A. Massa, "Multiple shapes reconstruction by means of multi-region level sets," IEEE Trans. Geosci. Remote Sensing, vol. 48, no. 5, pp. 2330-2342, May 2010.

[18] M. Benedetti, D. Lesselier, M. Lambert, and A. Massa, "A multi-resolution technique based on shape optimization for the reconstruction of homogeneous dielectric objects," Inverse Problems, vol. 25, no. 1, pp. 1-26, Jan. 2009.

[19] M. Salucci, D. Sartori, N. Anselmi, A. Randazzo, G. Oliveri, and A. Massa, "Imaging buried objects within the second-order Born approximation through a multiresolution-regularized inexact-Newton method", in 2013 International Symposium on Electromagnetic Theory (EMTS), (Hiroshima, Japan), pp. 116-118, May 20-24 2013.

[20] T. Moriyama, G. Oliveri, M. Salucci, and T. Takenaka, "A multi-scaling forward-backward time-stepping method for microwave imaging," IEICE Electronics Express, vol. 11, no. 16, pp. 1-12, Aug. 2014.

[21] P. Rocca, M. Carlin, L. Manica, and A. Massa, "Microwave imaging within the interval analysis framework," Progress in Electromagnetic Research, vol. 143, pp. 675-708, 2013.

[22] P. Rocca, M. Carlin, G. Oliveri, and A. Massa, "Interval analysis as applied to inverse scattering," IEEE International Symposium on Antennas Propag. (APS/URSI 2013), Chicago, Illinois, USA, Jul. 8-14, 2012.

[23] L. Manica, P. Rocca, M. Salucci, M. Carlin, and A. Massa, "Scattering data inversion through interval analysis under Rytov approximation," 7th European Conference on Antennas Propag. (EuCAP 2013), Gothenburg, Sweden, Apr. 8-12, 2013.

[24] P. Rocca, M. Carlin, and A. Massa, "Imaging weak scatterers by means of an innovative inverse scattering technique based on the interval analysis," 6th European Conference on Antennas Propag. (EuCAP 2012), Prague, Czech Republic, Mar. 26-30, 2012.